Master Thesis

Using moon observations to characterize infrared sounders on different satellites

Constanze Valerie Elisabeth Seibert

constanze.seibert@studium.uni-hamburg.de

M.Sc. Meteorology

Matr.-No. 7330921

Primary supervisor: Prof. Dr. Stefan Alexander Bühler

Secondary supervisor: Dr. Martin Jörg Burgdorf

Submission: 20 July 2022

Using moon observations to characterize infrared sounders on different satellites.

Shoot for the Moon. Even if you miss it, you will land among the stars.
– Oscar Wilde

Abstract

Observations of the Earth's atmosphere with sensors on a polar orbit employ a two-point calibration using a cold and a hot reference point. The hot reference point is an on-board blackbody target. The cold reference point is the deep space view (DSV). In case of the Moon being in the direction of the DSV, it provides an additional calibration target.

This work is based on an analysis of calibration scans from High-resolution Infrared Radiation Sounder (HIRS) on various satellites that have observed the Moon coincidentally with a focus on the water-vapor sensitive channel 12. Observations of the Moon enable a characterization of the sensor performance across different versions of the instrument. Following up on Burgdorf et al. [2020], who analyzed 20 Moon observations with phase angles near half Moon, I extend the analysis with a systematic search for every possible Moon intrusion of all satellites equipped with HIRS for channel 12. I identify 123 Moon observations on 16 different satellites in the time period from 1978 until 2021, which I use to characterize the performance of the HIRS sensor and to validate the thermo-physical model (TPM) of the Moon by Müller et al. [2021].

Based on well known infrared-relevant surface properties of the Moon, a TPM allows to calculate the temperatures of the sun-illuminated parts for the different helio-centric distances (0.981 to 1.019 au) with a TPM. The integration over the satellite-centric visible parts of the surface gives the total lunar flux at each HIRS observing epoch. These fluxes can be compared to fluxes measured by HIRS instruments, which have seen the Moon under different phase angles ranging from -85.4° to +82.6° with the nearest observation to full Moon at a phase angle of 1.4°. Hence, the HIRS disk-integrated fluxes, which are covering a wide range of phase angles and wavelengths, provide observational constraints on the TPM input parameters for the Moon, especially for the emissivity, albedo and thermal properties [Müller, 2002]. Such a tested and validated model solution for the Moon is needed to directly compare the flux calibration of future HIRS-like sensors to those that were operational decades ago.

There are a number of sources for the same instrument, which all give different values for the instantaneous field of view (FOV). Comparisons between observations and model calculations can help to clarify the estimation of the instantaneous FOV of the different channels. I found that the FOV varies slightly with wavelength, and between short-wave and long-wave channels for some satellites. In addition to that, the Moon observations show that the long-wave channels FOV is $(1.33 \pm 0.09)°$ for HIRS/2 on NOAA-12 and $(1.36 \pm 0.05)°$ for HIRS/3, respectively.

Contents

Acronyms

AAPP ATOVS and AVHRR Pre-processing Package

ATOVS Advanced TIROS Operational Vertical Sounder

au astronomical unit(s)

AVHRR Advanced Very High Resolution Radiometer

CrIS Cross-track Infrared Sounder

DSV deep space view

FORUM Far-infrared Outgoing Radiation Understanding and Monitoring

FOV field of view

GIIRS Geostationary Interferometric Infrared Sounder

HIRS High-resolution Infrared Radiation Sounder

IASI Infrared Atmospheric Sounding Interferometer

IR infrared

JPL Jet Propulsion Laboratory

Metop Meteorological operational

NOAA National Oceanic and Atmospheric Administration

rms root-mean-square

SEVIRI Spinning Enhanced Visible InfraRed Imager

SNO simultaneous nadir overpass

TIROS Television Infrared Observation Satellite

TPM thermo-physical model

UTH upper tropospheric humidity

1. Introduction

The study of climate variability and climate change requires long time series of satellite data that are well calibrated and homogeneous over time. Satellite data of this type are called Climate Data Records and are produced through careful recalibration and reprocessing [Roebeling et al., 2013].

The High-resolution Infrared Radiation Sounder (HIRS) instrument was initially designed for weather applications, where only moderate calibration accuracy is required. As the HIRS instrument has been mounted on more than a dozen satellites since 1975, the long time series of HIRS is very valuable for climate research. However, large biases of the brightness temperature of the HIRS channel 12, which is used to measure the upper tropospheric humidity (UTH), were found by Shi and Bates [2011]. The UTH is a fundamental climate data variable and a key component of the water vapour feedback [Held and Soden, 2000]. Gierens et al. [2018] also noticed a discontinuity in the time series of HIRS brightness temperature channel 12, which is caused by the transition from HIRS/2 to HIRS/3 in 1999 where the shift in the central wavelength of channel 12 from 6.7 to 6.5 μm is involved. Therefore, it is of great interest to identify and correct the systematic errors properly.

Different approaches to correct inter-satellite biases already exist. For example, Cao et al. [2005] and Shi et al. [2008] approach inter-satellite calibration for HIRS based on simultaneous nadir overpass (SNO) observations of different satellites to inter-compare radiances measured by HIRS channels. Buehler et al. [2020] present a complementary inter-calibration method to simultaneous nadir overpasses, called opportunistic constant target matching, where a geostationary infrared (IR) sensor is used to select constant target matches in warm reference regions. These approaches aim to reduce the uncertainty among the satellites, but the methods are only applicable for satellites that are operating coincidentally.

Using a model of the Moon for calibration has clear benefits over previous methods, because the Moon can be used as an absolute flux standard. The Moon observations are useful to characterize the HIRS instrument and to validate the model. The surface of the Moon exhibits long-term stability and appears suitable as a candidate for a thermal calibration source [Liu and Jin, 2022]. The Moon is already used for calibration of instruments in the optical (see Kieffer and Wildey [1996]) and the microwave (see Hu et al. [2015] and Burgdorf et al. [2016]) regime. The infrared-relevant surface properties of the Moon are well known, so it is also possible to use the Moon for the calibration of IR sensors. The Diviner IR radiometer onboard the Lunar Reconnaissance Orbiter measured

the IR brightness temperature of a small region of the Moon at nadir observations [Liu and Jin, 2022]. With HIRS it is possible to see the complete lunar nearside and therefore get disk-integrated measurements of the Moon. The disk-integrated properties of the Moon are constant in previously analyzed observations (see Burgdorf et al. [2020]), while the temperature of the Moon varies with the illumination of the Sun. By establishing the Moon as an absolute flux standard, it will become possible to clear climate data records from artificial, non-climatic effects that are common to all instruments of a certain type and that can therefore not be identified by postlaunch matchups.

During observations of the Earth's atmosphere, the HIRS instrument enters a calibration mode every four minutes. Besides one or two internal calibration targets onboard the satellite, the instruments performs a deep space view (DSV) scan. Sometimes the Moon appears in the calibration view of the DSV. These space views are not taken into account for the calibration procedure. However, the Moon itself provides an additional calibration target. In this work, an explicit search for lunar observations during the calibration scans is carried out. Filter criteria are set to find and select Moon observations, where the Moon was fully included in the FOV of the instrument. The primary objective of this work is to improve the characterization of the long history of HIRS sensors on various satellites using the Moon as a calibration target. In addition, the results of this work contribute to an improved radiative model of the Moon, which can be used also for the calibration of future HIRS-like sensors.

In Chapter 2, the instrument properties of the HIRS are listed, while the differences between the versions of HIRS are discussed. In addition to the instrument, a brief description of the thermo-physical model (TPM) is given. The used method of how to find and analyze the Moon observations, which appear during the calibration scans of the HIRS instrument, is described in Chapter 3. The results are presented and discussed in Chapter 4 with a special focus on the results of channel 12 and the comparison of the measurements with the model calculations. I conclude all findings and give an outlook in Chapter 5.

2. Instrument and data

2.1. The High-resolution Infrared Radiation Sounder

The High-resolution Infrared Radiation Sounder (HIRS) is a discrete stepping line-scan instrument and was developed to obtain information on the atmospheric vertical profile from the Earth's surface to about 40 km altitude [Robel and Graumann, 2014]. HIRS has been flown on various satellites on polar orbit since 1975.

A polar-orbiting satellite is placed in a circular sun-synchronous orbit, typically at a low altitude of 700 to 900 km. Most often these satellites cross the equator every day at the same local solar time, once ascending (from south to north) and once descending. The equatorial crossing times remain nearly constant throughout the year. However, deterioration of the orbit may cause a slow change in the value over time. Figure 2.1 demonstrates the ascending node crossing time for the satellites equipped with HIRS. The Meteorological operational (Metop) satellites are in controlled orbits to prevent substantial drifts in crossing times.
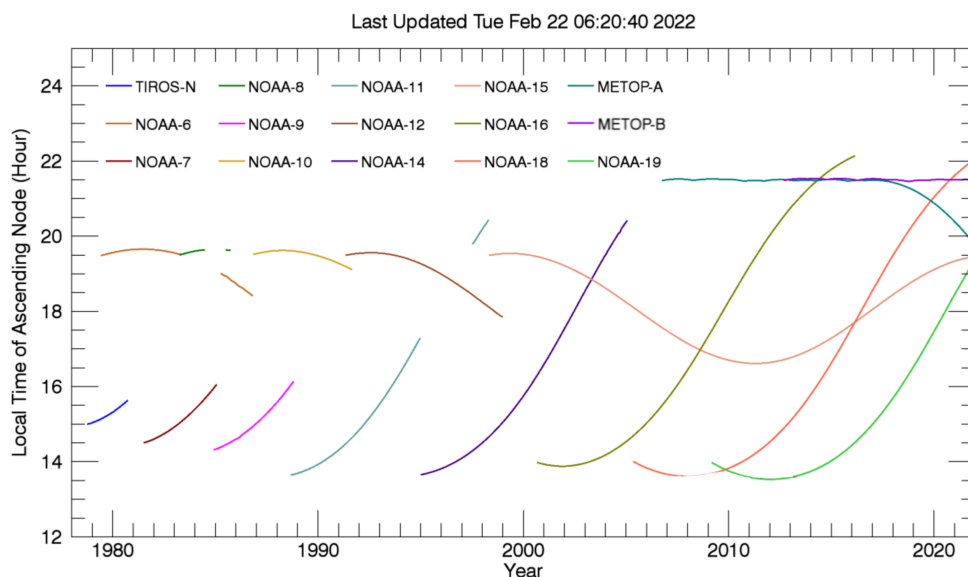

Figure 2.1.: The local ascending node crossing time for all satellites equipped with HIRS instrument. Image taken from Remote Sensing Systems [2022].

Instrument	Satellite	Start	End
HIRS/1	Nimbus-6	Jun 1975	Mar 1983
HIRS/2	TIROS-N	Oct 1978	Feb 1981
HIRS/2	NOAA-6/A	Jun 1979	Mar 1987
HIRS/2	NOAA-7/C	Jun 1981	Jun 1986
HIRS/2	NOAA-8/E	Mar 1983	Dec 1985
HIRS/2	NOAA-9/F	Dec 1984	Feb 1988
HIRS/2	NOAA-10/G	Sep 1986	Aug 2001
HIRS/2I	NOAA-11/H	Sep 1988	Jun 2004
HIRS/2	NOAA-12/D	May 1991	Aug 2007
HIRS/2I	NOAA-13/I	Oct 1993	Oct 1993
HIRS/2I	NOAA-14/J	Dec 1994	May 2007
HIRS/3	NOAA-15/K	May 1998	
HIRS/3	NOAA-16/L	Sep 2000	Jun 2014
HIRS/3	NOAA-17/M	Jun 2002	Apr 2013
HIRS/4	NOAA-18/N	May 2005	
HIRS/4	NOAA-19/N'	Feb 2009	
HIRS/4	Metop-A	Oct 2006	Nov 2021
HIRS/4	Metop-B	Sep 2012	

Table 2.1.: List of satellites equipped with HIRS sensor and operational lifetime. Values from WMO OSCAR [2022].

The following information is collected from various technical reports on the HIRS instrument. The main sources corresponding to HIRS version 2 are several reports by Koenig et. al. [1975, 1979], Koenig [1980] and the NOAA Polar Orbiter User's Guide by Kidwell [1995]. For HIRS version 3 and 4 the main source of information comes from the KLM User's Guide by Robel and Graumann [2014].

Table 2.1 lists every satellite equipped with a HIRS sensor, along with the instrument version and the period of the mission. The first HIRS instrument was developed and flown in 1975 on the Nimbus 6 satellite. The basic design for the Nimbus HIRS system was modified for the Television Infrared Observation Satellite (TIROS)-N series of spacecraft to improve the sensor performance [Robel and Graumann, 2014]. This HIRS/2 design was used in the Protoflight Model on TIROS-N and Flight Model 1 on NOAA-06 [Koenig et. al., 1979] and was further improved for the satellites NOAA-C to NOAA-G (NOAA-07 to NOAA-10 and NOAA-12). Some adjustments were made and three HIRS/2I units were built, which flew on the satellites NOAA-H to NOAA-J (NOAA-12, NOAA-13 and NOAA-14). Additional improvements and operational changes were made for the HIRS/3. Three HIRS/3 instruments were built for use on the National Oceanic and Atmospheric Administration (NOAA) KLM spacecraft, which stands for NOAA-15, NOAA-16 and NOAA-17. The HIRS/4 design is a modification of the HIRS/3 design, built to fly on the NOAA-N and NOAA-N' spacecraft, which stands for NOAA-18 and NOAA-19 [Robel and Graumann, 2014]. The HIRS/4 is also equipped on the first two Metop satellites, Metop-A and Metop-B.

The HIRS sensor receives radiation of the visible and IR spectrum through a single tele-scope. An elliptical scan mirror provides cross-track scans of 56 increments of 1.8 de-grees. With the help of a rotating filter wheel, 20 narrow radiation channels are se-lected. The mirror steps rapidly (<35 msec), then holds at each position while the 20 filter segments are sampled. This action takes place each 100 msec [Robel and Graumann, 2014]. Optical registration of all channels is achieved by splitting the bands into two optical paths [Koenig et. al., 1979], which is shown in Figure 2.2. The collected energy is separated by a beam splitter into long-wave (above 6.5 μm) and short-wave (below 6.5 μm), then passed through field stops and through a rotating filter wheel to cooled detectors [Koenig et. al., 1979]. In the short-wave path, a second beam splitter separates the visible channel and directs it to a silicon detector. By that, one silicon cell detects energy through the visible channel at 0.69 μm (28 in Fig. 2.2), one indium antimonide detector (23 in Fig. 2.2) collects energy in seven short-wave channels from 3.7 to 4.6 μm and one mercury cadium telluride detector (13 in Fig. 2.2) measures the energy in twelve long-wave channels between 6.5 to 15 μm [Koenig, 1980]. Each channel measures en-ergy over a frequency bandwidth, which is integrated over the bandwidth to get a center frequency. For this work, only the IR measurements are relevant, thus only the spectral characteristics of all IR channels for each satellite are listed in the Appendix A.1. The central frequency of the channels are similar for all HIRS versions, except for channel 10 and channel 12. For HIRS/2 the center frequency of channel 10 is 8.2 μm, while for HIRS/2I it is changed to 12.5 μm. HIRS/3 measures a center frequency of 12.4 μm and HIRS/4 also measures 12.5 μm for channel 10. The central wavelength of channel 12 for HIRS/2 and HIRS/2I is 6.7 μm and was changed for HIRS/3 and HIRS/4 to 6.5 μm. The channels 13-16 have very similar wavelengths between 4.4 and 4.6 μm and the central wavelengths of the channels 1-7, which lie between 13.3 and 15 μm, are also very close to each other.

The following information is taken from Koenig et. al. [1975]. The size of the FOV changed with the version of HIRS. The HIRS/1 system has been designed for the field stop to completely define the FOV and the registration between bands. However, FOVs of 1.24° were measured instead of the planned 1.5°. The major cause of the discrepancy was determined to be the antireflection coating on the outer radius of the aplanat. It was found that this coating can affect the FOV. So the optical FOV measures 1.28° for the visible, 1.24° for short-wave and 1.17° for long-wave.

In the following, the information is taken from Koenig et. al. [1979]. For the first HIRS/2 satellites, some modifications were made. Major items that were changed are the scan mirror, telescope, visible detector, some spectral filters and some optic elements. Optical analysis verified that the detector and aplanat both have large numbers of rays striking their surfaces at high incidence angles. Thus, the surface antireflective coating of the detector was changed for TIROS-N and NOAA-06 accordingly to aid collection of high incidence angle rays. A program was started to define and change the coating on the

aplanatic lens that mounts to the detector. From NOAA-07 onwards, the improved detector surface and improved aplanat surface was implemented on the HIRS/2 instrument. The ground test data for TIROS-N and NOAA-06 are showing FOV values, which are wavelength dependent and measured to be between 1.16° and 1.24° for the IR channels (see Table A.3 and Table A.4). The channel-to-channel registration is 0.05° in the long-wave and 0.02° in the short-wave band.

Kidwell [1995] states that the optical FOV is 1.25° for all HIRS/2. This stands in contrast to Burgdorf et al. [2020], who calculated the ratios of Moon intrusions with HIRS/2 and HIRS/3 as well as with HIRS/2 and HIRS/4 and came to the result, that the FOV of newer satellites equipped with HIRS/2 is $(1.4 \pm 0.03)°$.

Robel and Graumann [2014] state, that the instantaneous FOV for HIRS/3 for each channel is approximately 1.4 degrees in the visible and short-wave IR and 1.3 degrees in the long-wave IR band. Burgdorf et al. [2020] calculated that the FOV for HIRS/3 is $(1.3 \pm 0.03)°$.

Ground test data for the Metop satellites of HIRS/4 measure FOV values roughly of 0.7° for all channels, but slightly dependent of the wavelength (see Table A.17 and Table A.18) [ITT Exelis, 2012].

In Chapter 4.2.5 it will be investigated, which values for the FOV are assumed to be correct and whether there is a non-negligible wavelength dependency.
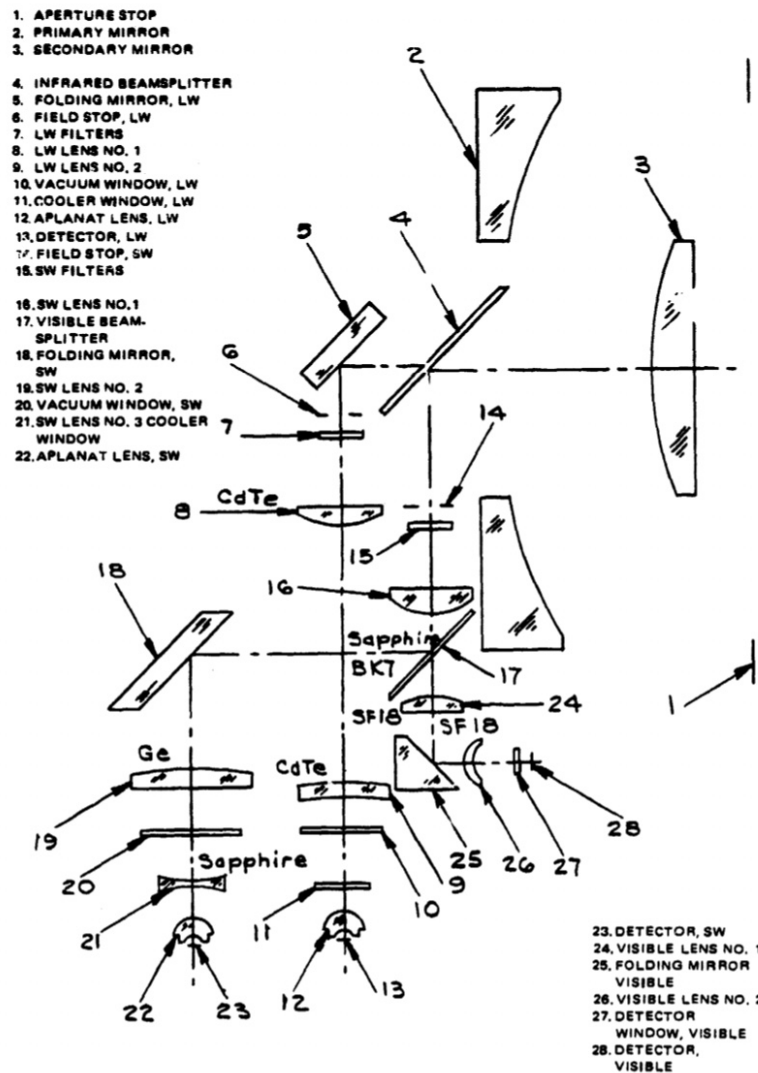
Figure 2.2.: Optics of HIRS instrument. Figure from Koenig et. al. [1979].

2.1.1. Calibration of the High-resolution Infrared Radiation Sounder

Remote sensing systems create a two-dimensional image of the ground by scanning perpendicular to the direction of movement of the aircraft or satellite. This is achieved by using a linear array of many detectors to record each scan line at the same time.

The HIRS instrument can be commanded to automatically enter a calibration mode. When the instrument is in calibration mode, the mirror starts from the beginning of a scan line to slews to a space view and samples all channels for the equivalent time of one complete scan line of 56 scan steps. Next, the mirror is moved to a position where it views a cold calibration target and data is taken for the equivalent of 56 scan steps. Then the mirror is stopped to a view of on an internal warm target for another 56 scan steps. After the completion of the calibration mode, the mirror continues its motion to the position where it begins the normal Earth scan [Kidwell, 1995].

The data from these views provide sensitivity calibrations for each channel every 40 scan lines at 256 second intervals [Robel and Graumann, 2014]. Figure 2.3 visualizes the scan line positions of a HIRS like sensor. The HIRS/2 instrument proceeds with a three point
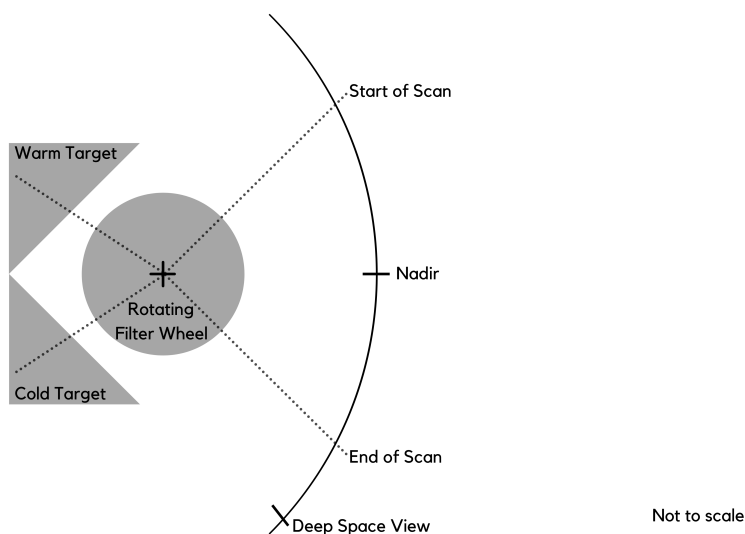

Figure 2.3.: Scan position of HIRS. Simplified from Koenig et. al. [1979].

calibration scan, using programmed views of three radiometric targets, after every Earth scan. So after after a sequence of twenty scan lines on Earth the FOV moves to a DSV and then to the other radiometric targets. A warm blackbody target mounted on the base of the instrument operates at around 290 K and the cold target isolated from the instrument operates at around 265 K [Koenig et. al., 1975]. For later HIRS/2 versions the cold blackbody target is no longer used. Therefore, the IR calibration for HIRS/3 and HIRS/4 is provided by programmed views of only two radiometric targets: the warm target on the instrument base and the DSV. For HIRS/2, HIRS/2I and HIRS/3 four internal warm target temperature sensors measure the temperature of the on-board warm calibration target. For HIRS/4 a fifth internal warm target temperature sensor was included to monitor the temperature of the warm target [Robel and Graumann, 2014].

Moon in the field of view of the calibration scan

Sometimes the Moon appears in the FOV of the satellite during the DSV calibration scan. Normally, these observations can no longer be used for calibration, but they are now being filtered for that a third flux value can be taken from them to calibrate the instrument. Kieffer and Wildey [1996] were the first, who suggested to use the Moon itself as radiometric standard for the calibration of satellite instruments.

Seen from the satellite, the Moon appears at an angle of about half a degree, while its apparent diameter varies slightly depending on its distance from Earth. The FOV of the satellite varies for the version of HIRS between 0.7° and 1.4°. This means, that when the

Moon appears in the DSV of the satellite, the Moon is smaller than the FOV of the satellite. Figure 2.4 visualizes the variation of the FOV with the version of HIRS. The newer the version of HIRS the smaller the FOV.
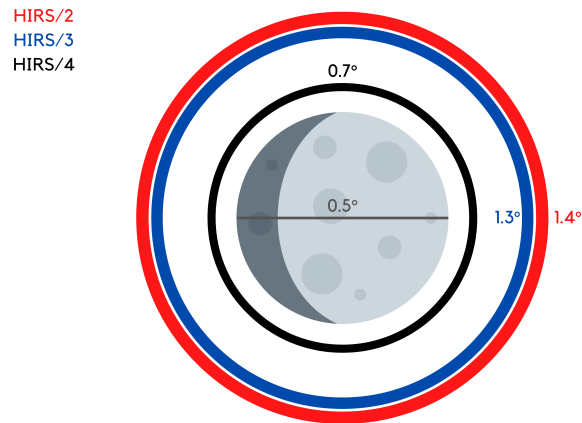
Figure 2.4.: FOV of HIRS in comparison to the apparent angle of the Moon. Seen from the satellite base, the Moon appears at an angle of 0.5°. The FOV of the satellite varies for the version of HIRS between 0.7° and 1.4°. FOV values taken from Burgdorf et al. [2020].

2.2. Thermophysical model

A model of the Moon is used to interpret the measured fluxes and compare them with model fluxes. The TPM used for a validation and comparison in this study was developed by Lagerros [1996, 1997, 1998], Müller and Lagerros [1998, 2002], and Müller [2002]. In the following, the most important information about the TPM is summarised. For a more comprehensive overview see Müller et al. [2021].

The model can make predictions of objects' surface temperatures, disk-integrated flux densities in the thermal-wavelength regime, or thermal lightcurves for aspherical bodies or objects with albedo variations. The TPM predicts the thermal emission of atmosphereless bodies in the IR to microwave regime and has been used in the last two decades for near-Earth asteroids, main-belt asteroids, satellites and trans-Neptunian objects. The TPM can give diameters, albedo values and thermal properties via the interpretation of disk-integrated thermal measurements in cases where the available thermal data have good quality, cover wide spans of time, wavelengths and phase angles. The model considers the true position of the object with respect to the Sun and the observer.

The Earth's distance to the Sun varies with the Earth's orbit around the Sun in 365.25 days. The Earth's orbit and the Moon's orbit with their minimum and maximum distances to their host are visualized in Figure 2.5. The minimal distance of the Earth to the Sun is reached in January and is called perihelion at a heliocentric distance $r = 0.9833$ au. The maximal distance is reached in July and called aphelion at $r = 1.0167$ astronomical unit(s) (au), while the mean distance is $r = 1$ au. The Moon orbits the Earth within 27.3 days, while the minimal distance is called perigee and the maximal distance apogee. It is assumed that the brightness temperature of the Moon varies with the distance of the Moon to the Sun.

To predict the thermal emission of the Moon the TPM does three steps:

1. Estimation of the temperature of each surface element over the entire Moon. Figure 2.6 shows a calculated temperature map at -90° phase angle. For the calculation of the temperature the model needs the surface albedo A, the heliocentric distance r and the solar constant (1361 Wm^{-2} at 1 au from the Sun).
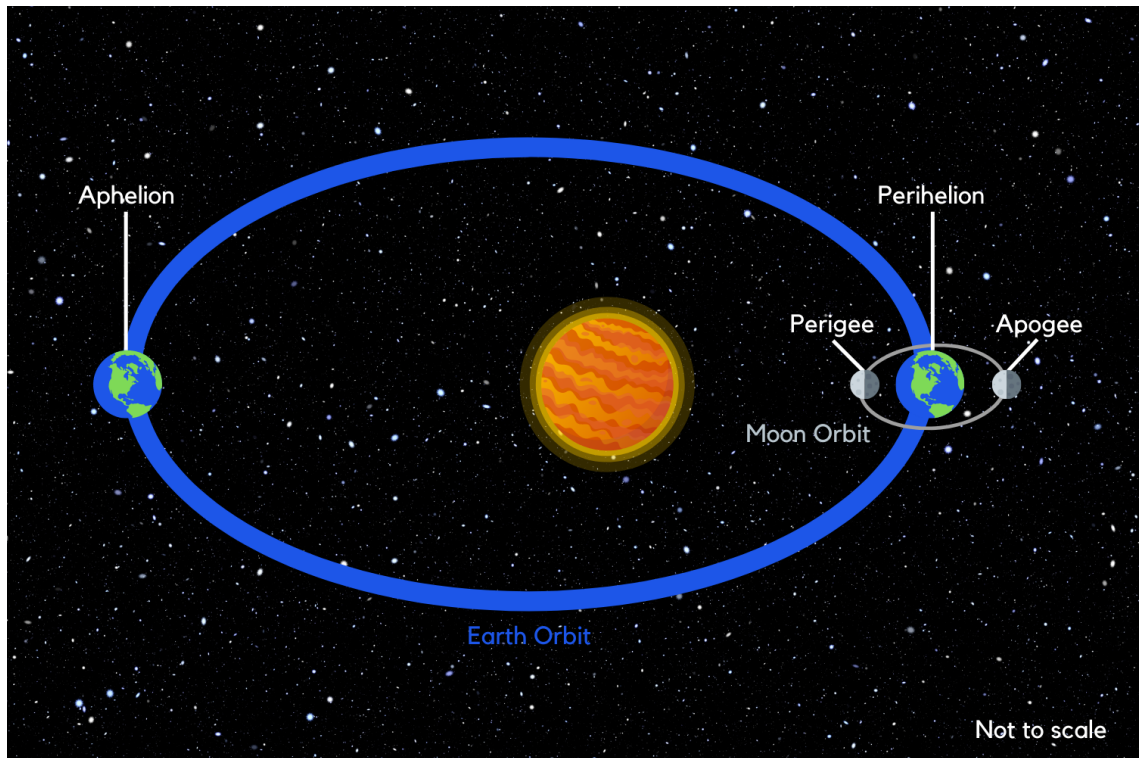
Figure 2.5.: Orbits of Earth and Moon with their minimal and maximal distances to their host. Inspired by an image on Universe Today [2022].
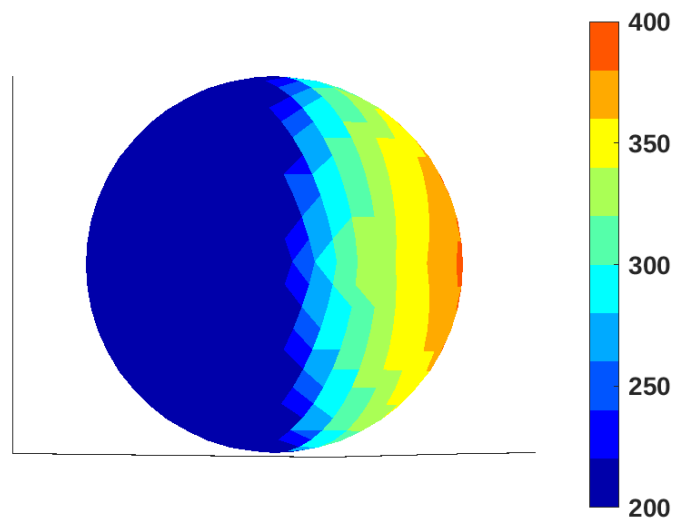

Figure 2.6.: Temperature map (in Kelvin) of the Moon at -90° phase angle at the minimal Sun-Moon distance with calculated values from the TPM.

2. Calculation of the intensity I_λ of each surface element in the direction of the observer, as:

$$I_\lambda = \epsilon_d \frac{B_\lambda(\gamma T)}{\pi} + I_{sc} + I_{ref}, \tag{2.1}$$

where B_λ is the Planck function and T is the temperature of the surface. In the vicinity of the full Moon the opposition effect plays a role, which is mostly called "beaming effect" in the IR regime. γ is representing the beaming function, which describes the thermal emission towards the Sun originating from the surface roughness. At full Moon we look directly into the craters and see the warm crater bottom, which is additionally warmed by the crater rims. Rough surfaces almost always show this effect. For more details on the calculation of the beaming function see Lagerros [1996]. ϵ_d represents the direction- and wavelength-dependent emissivity, whereby $\frac{\epsilon_d}{\pi}$ is the hemispherical spectral emissivity. For the calculation of the direction- and wavelength-dependent emissivity, the TPM considers sub-surface scattering processes. To the first term of the intensity the multiple scattered radiation I_{sc} and the reflected solar radiation I_{ref} are added. The reflected sunlight calculations are implemented by using Lambert's scattering law, but the calculations are not tested in the transition region between reflected light and thermal emission, where non-linear effects are involved.

3. Determination of the disk-integrated flux F_λ, defined as:

$$F_\lambda = \frac{1}{\Delta^2} \oint I_\lambda(S)\mu dS, \tag{2.2}$$

where Δ represents the observer's distance, dS the surface element, $I_\lambda(S)$ the corresponding intensity of the surface element towards the observer and μ the projection of the surface element towards the observer.

The thermal emission of an idealized flat surface deviates from a macroscopically rough one due to partial shadowing, sunlight scattering and self-heating. These effects cause small areas of higher temperatures and more thermal radiation to be emitted toward the Sun, known as the thermal IR beaming effect. The surface roughness is modeled by hemispherical segments and controlled by specifying the root-mean-square (rms) of surface slopes.

There are first studies comparing 22 HIRS lunar observations with this thermo-physical model (TPM) that show excellent agreement (3% in the long-wave channels and 8% in the short-wave channels, see Müller et al. [2021]) when using the following model parameters:

- a thermal inertia $\Gamma = 55\ \mathrm{Jm^{-2}K^{-1}s^{-1/2}}$

- a surface roughness characterized by an rms slope of 32°

- an albedo of $A = 0.10$

- a lunar global hemispherical spectral emissivity model with $\epsilon = 0.69$ at 4.5 μm and increasing values close to $\epsilon = 1.0$ at 12 μm

- phase-angle asymmetry model corrections of up to 3% at $\pm$ 60° for wavelengths >6 μm.

Since the TPM generates thermal properties for cases where the available thermal data is of good quality and covers large time periods, new HIRS measurements of the Moon are valuable for validating the model [Müller et al., 2021]. In this work, the complete data set of all lunar measurements with HIRS will be compared with this TPM in Chapter 4.2. The radiance output of the TPM is in Jansky and need to be converted to $\frac{MJy}{sr}$ for a comparison with the HIRS values. The angular size of the Moon a in steradian is calculated from the angular diameter of the Moon α in degree, like this:

$$a = \pi \left(\frac{\alpha \cdot 3600}{2} \right)^2 \cdot 2.3504 \cdot 10^{-11}. \tag{2.3}$$

Thus, the model output will be converted with $R / \frac{MJy}{sr} = \frac{R \cdot 10^{-6} / Jy}{a / sr}$.

3. HIRS data extraction

To use the Moon as a third calibration standard it must appear in the field of view (FOV) of the satellite. As already explained in Chapter 2.1, HIRS proceeds with a calibration scan after a sequence of twenty scan lines on Earth. The deep space view (DSV) of a polar orbiting satellite points at a direction close to the orbital axis of the satellite near the celestial equator. This means that occasionally the Moon appears in the DSV of the calibration scan, but for satellites equipped with a HIRS like sensor it is only possible to see the Moon between -90° to +90° phase angle. Figure 3.1 visualises the FOV direction of a polar orbiter during the DSV calibration scan, which is always away from the Sun. It is also possible that only Earth scenes were observed when the Moon crossed the direction of the DSV, or that only a part of the Moon is in the FOV. As a result, an entire year may pass without a single useful lunar observation [Burgdorf et al., 2020]. As most satellite orbits drift occasionally, the local equator crossing time changes (see Figure 2.1), and therefore it is possible to see the Moon at very different phase angles with the same satellite.

Data from HIRS/2, HIRS/2I, HIRS/3 and HIRS/4 from October 1978 until December 2021 was analyzed. Data from HIRS/1 on Nimbus-6 has not been taken into account for this study due to lack of digitization and format differences of the data. For the analyzation of the Moon observations, the HIRS Level 1b data provided by the NOAA Comprehensive Large Array-data Stewardship System was used, because it provides raw instrument counts. Since the observations of the Moon are not part of the standard processing, the raw data had to be processed and calibrated. To retrieve the radiometric data, the KLM User's guide [Robel and Graumann, 2014] recommends to read the data as a signed 2 byte integer and then subtract 4096. The resultant value should be between -4095 and +4096. The filter wheel rotates and filters the 20 channels in the following order: 1, 17, 2, 3, 13, 4, 18, 11, 19, 7, 8, 20, 10, 14, 6, 5, 15, 12, 16, 9 [Robel and Graumann, 2014]. Due to the circuitry, lower count values indicate higher incoming flux, which means that we look for the lowest count values in the DSV scan lines, since this is the highest incoming flux possibly from the Moon. After processing in the amplifier chains and before analog-to-digital conversion, the signal is already reversed [Koenig et. al., 1979].

3.1. Filtering for Moon intrusions on HIRS

In order to use the Moon intrusions for calibration, one needs to find and select them properly. An automated process with Python was developed by employees of the uni-
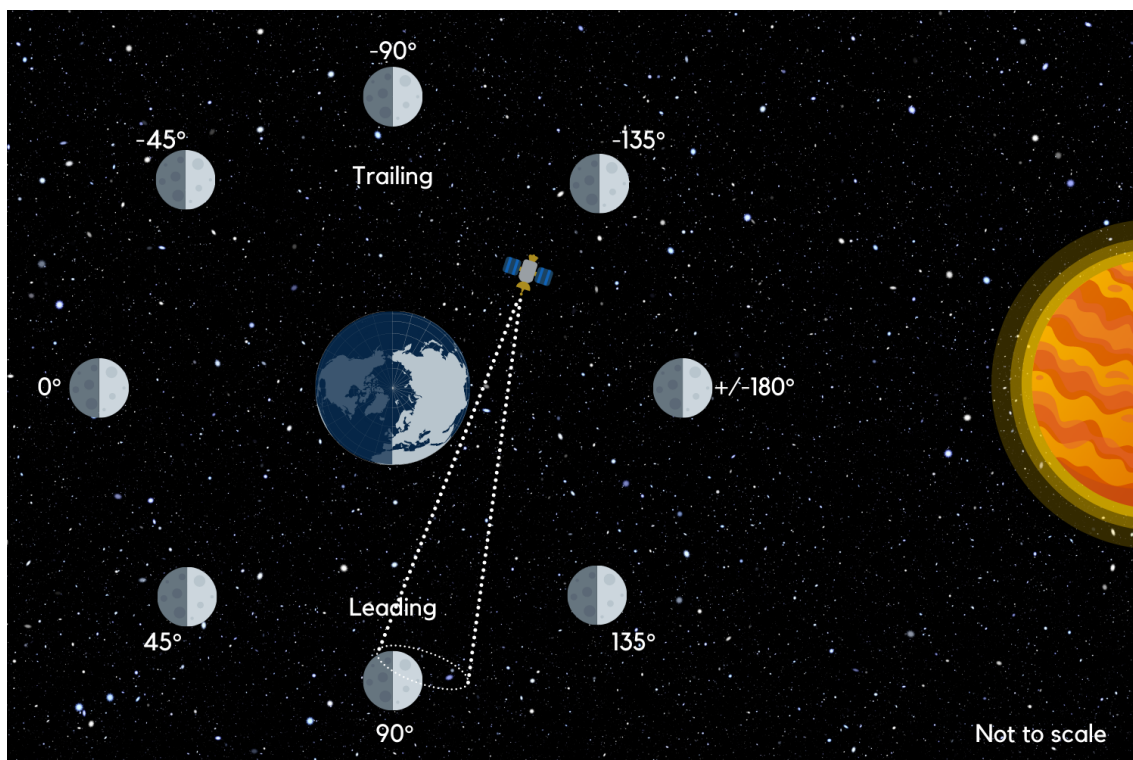
Figure 3.1.: Observable Moon phases in DSV of polar orbiting satellites. For the polar
orbiting satellites, Moon phases from -90° to +90° are visible, because the DSV
is always away from the Sun. Image inspired from illustration on Astronomy
Notes [2022].

versity of Hamburg, namely Marc Prange and Maximilian Ringel using Typhon [Lemke
et al., 2021] to read and process the HIRS data. During this thesis I took the existing
program as a basis and developed it in further detail. The source code can be found on
Github [1] with a small documentation.

The program loops through all HIRS observation files given for the specified satellite,
channel and time period. For each of these files it checks if two conditions are fulfilled
and gives an overview plot if the conditions are fulfilled, like shown in Figure 3.2 for
channel 8 on NOAA-14 on 8th of December 1997.

First, the program checks how large the gradient in between DSV scan lines is. If this gra-
dient between the DSV scan lines is larger than 50 (photon) counts, there could be either
a Moon intrusion or an instrumentation error. To find the possible Moon intrusion, the
program selects the scan line with the minimum averaged counts. This scan line should
include the Moon intrusion (intrusion-scan line).

One output example given from the program for a possible Moon intrusion is shown in
Figure 3.2. The color plot on the left visualizes all DSV scan lines of one observation file.
The scan line with the minimum average counts in comparison to the other scan lines is
then selected as possible Moon intrusion. For the calculation of the radiance, the differ-

---

[1]`https://github.com/atmtools/HIRS-Moon-Intrusions/tree/main`

ence of the counts during the Moon intrusion to the blackbody counts and the difference to the DSV before and after the intrusion are important. Therefore, the overview in Figure 3.2 shows from left to right all calibration scan lines of one observation file with their time against the scan position, the counts of the scan line before the possible Moon intrusion against the scan position, the counts of the scan line during the Moon intrusion against the scan position, the counts of the scan line after the possible Moon intrusion against the scan position and the blackbody counts of during the possible Moon intrusion against the scan position. From this point on, the program was extended for this work.
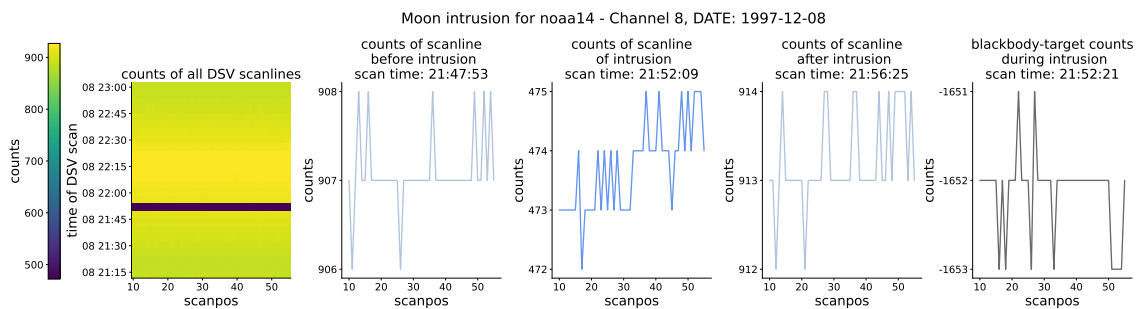
Figure 3.2.: Moon intrusion overview plot for channel 8 on NOAA-14 on 1997-12-08. From left to right: All calibration scan lines of one observation file with their timestamp against the scan position, the counts of the scan line before the possible Moon intrusion against the scan position, the counts of the scan line during the Moon intrusion against the scan position, the counts of the scan line after the possible Moon intrusion against the scan position and the blackbody counts during the possible Moon intrusion against the scan position.

To exclude instrumentation errors, the mean value of the DSV should not be constant over the whole scan period and should not have the value -4095 or +4096 [Robel and Graumann, 2014]. In order to filter for Moon intrusions, where the Moon was fully inside the FOV, the program checks that the difference of the mean value before and after the intrusion scan line is greater than 150 counts. The value was chosen on the basis of a Moon intrusion, where the phase angle of the Moon was -85.4° and the mean count difference of the DSV scan lines was 214 counts. The difference Δ is defined like this:

$$\Delta = \left| \overline{X}_{DSV,\,before/after} - \overline{X}_{Moon} \right|,$$

while $\overline{X}_{Moon}$ is the mean value of the scan during a Moon intrusion and $\overline{X}_{DSV,before/after}$ the mean value of the DSV before or after the Moon intrusion. If the Moon is in the FOV of the satellite during the calibration scan, the signal can change within 6.4 seconds, because the Moon is either moving in or outside of the FOV [Burgdorf et al., 2020]. When the signal stays constant, the Moon is fully included in the FOV. To make sure that the Moon is fully inside the FOV, an additional filter criterion was set. It was checked if

the standard deviation of the counts during the Moon intrusion is less than 5 counts. These filter criteria were tested for channel 8, because this channel has the lowest noise equivalent delta radiance (see A.1 and A.2) and for channel 12, because it is of the highest interest for this study. This means that the Moon might have not been fully included in other channels, since the channels can have systematic pointing differences (analyzed by Burgdorf et al. [2020]). Nevertheless, all 19 IR channels are checked for plausible values and plotted like shown in Figure 3.3. The selected scan range reaches from scan position 10 to scan position 56. In principle it observes each 56 times, but the first 8 views are very often contaminated by the spacecraft while the mirror is still swinging to the right position [Holl et al., 2019]. In practice only 48 views are useable most of the time and that is why the scan range is selected from position 10 to 56. With Figure 3.3, it is possible to check whether the Moon was completely inside the FOV during the whole scan time period for all channels. Usually the Moon does not remain in the FOV for the entire duration of the calibration scan. Therefore, it is possible to select the scan position range for each channel separately. For Figure 3.3 (a), the count variations are small and partly resulting from the digitization noise (see channel 17, 18 and 29). Figure 3.3 (a) shows a Moon observation on 8th December in 1997, where the Moon was fully included in the FOV of most of the channels during the complete scan range. The selected range, where the Moon is assumed to be fully included, is marked with two vertical red dashed lines. This means, for the intrusion on 8th December in 1997 the complete scan range from 10 to 55 was selected for the channels 1-7, 10-11 and 17-19, while for channel 8 and 9 the selected range is from scan position 10 to 35, for channel 13 is 30 to 55, for channel 14 is 25 to 55 and for channel 15 and 16 is 20 to 55. The range should be chosen that at least 10 scan positions with the lowest constant counts are selected. and if it is not the case the corresponding channel will be excluded for the further analysis. Figure 3.3 (b) is an example of a Moon observation on 7th January of 1998, where the Moon was moving out of the FOV of most channels. Therefore, the scan range between 10 to 20 was selected and it was assumed that the Moon was fully included in this range.

The selected range is also taken into account for the calculation of the radiance, which is demonstrated in the following.
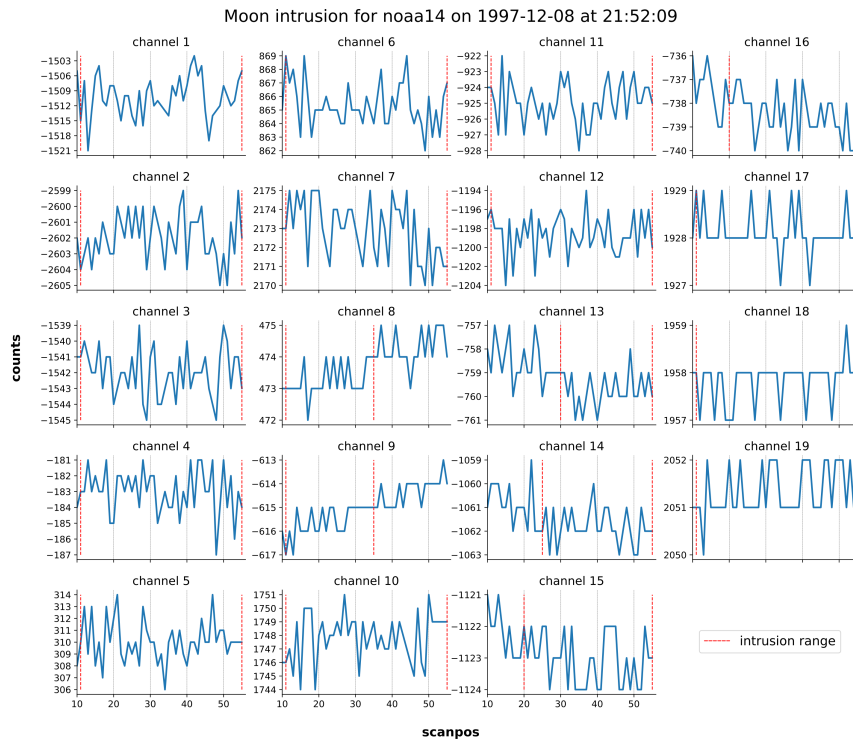
(a) Moon completely inside the FOV for most of the channels during the whole scan time.
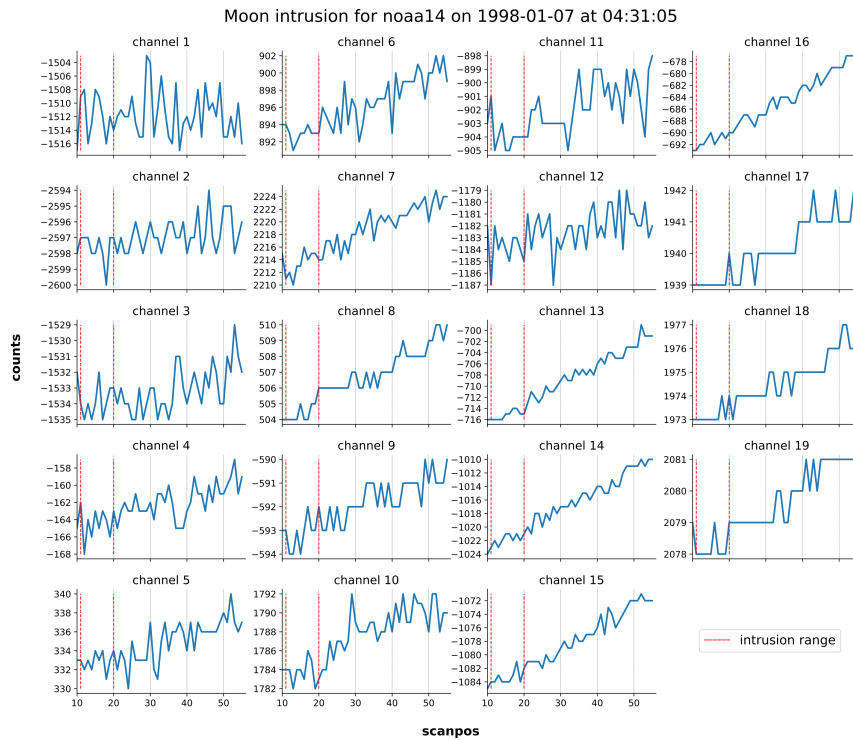
(b) Moon moving outside the FOV, but still inside the FOV from scan position 10 to 20.

Figure 3.3.: Example of two Moon intrusions on NOAA-14 with lightcurves for all 19 IR channels. The count values during the intrusion of the Moon in the FOV against the scan position of the instrument is plotted for each of the IR channels in blue solid lines. The red vertical dashed lines indicate the selected intrusion range, where the counts are more or less constant and it is assumed the Moon was fully inside the FOV.

3.2. Calculation of radiance and brightness temperature of the Moon

Each of the 19 IR channels have other counts values during the scan time, see Figure 3.3. This is also the reason why a comparison from each scan line views with the scan line before and after the Moon intrusion is needed for every channel. According to AAPP (Advanced TIROS Operational Vertical Sounder (ATOVS) and Advanced Very High Resolution Radiometer (AVHRR) Pre-processing Package) [Labrot et al., 2011], the radiance is assumed to be related to the count values through a quadratic equation:

$$R = a_0 + a_1 X + a_2 X^2, \tag{3.1}$$

with X representing the output in (photon) counts and a_0, a_1 and a_2 are calibration coefficients. Labrot et al. [2011] assumes that a_2 is computed before launch and is an unchanging characteristic for each channel. The calibration coefficients a_0 and a_1 are determined from equation 3.1 for the DSV and the blackbody counts and with the assumption that the radiance of the DSV is zero [Labrot et al., 2011].

For the radiance of the Moon, the mean value of the counts before and after the Moon appeared in the FOV of the DSV is taken, symbolized as $\overline{X}_{DSV}$. In addition to that, the mean counts of the blackbody target $\overline{X}_{bb}$ nearest to the time of the Moon intrusion of the satellite as well as the mean value of the selected constant region were chosen, where the Moon is in the FOV itself with $\overline{X}_{Moon}$. By using the average of the counts from the DSV calibration lines before and after, the influence of temperature changes originating from the instrument itself is minimized. Burgdorf et al. [2020] previously verified that the absence of a self-emission model adds an uncertainty of one or two counts to the cold calibration reference, but does not introduce a systematic error. A non-linearity term was not taken into account because there is no agreement on the correct values for this term and it is also set to zero in AAPP [Labrot et al., 2011].

$$R_{Moon} = R_{bb} \cdot \left(1 + \frac{(\overline{X}_{Moon} - \overline{X}_{bb})}{(\overline{X}_{bb} - \overline{X}_{DSV})}\right) \cdot \frac{FOV^2}{\alpha^2 \cdot 0.97} \tag{3.2}$$

Equation 3.2 gives the calculation of the radiance of the Moon R_{Moon} in $\frac{\text{MJy}}{\text{sr}}$. Besides the relation of the count values, the field of view FOV of the satellite in degrees, the apparent angular diameter of the Moon α in degrees and the radiance of the blackbody R_{bb} in $\frac{\text{MJy}}{\text{sr}}$ are important for the calculation of the radiance of the Moon. The factor 0.97 results from the energy, which is assumed to be 97% included in the FOV [Koenig, 1980]. The radiance of the blackbody is calculated according to Planck's law:

$$R_{bb} = \frac{c_1 \nu^3}{\left(e^{\frac{c_2 \nu}{T_{bb}}} - 1\right)}, \tag{3.3}$$

with the temperature of the blackbody T_{bb} in K, ν as the central wavenumber of the channel in cm^{-1}, and the constants $c_1 = 1.19 \cdot 10^{-5} \frac{\text{mW}}{\text{m}^2 \, \text{sr} \, \text{cm}^{-1}}$ and $c_2 = 1.44 \cdot 10^{-2}$ K m. According to Kidwell [1995] a band correction algorithm must be applied to the results of the inverse Planck equation, which is done with:

$$T_{bb}^* = b + c \cdot T_{bb}, \tag{3.4}$$

where b and c are band correction coefficients specific for each channel and provided by AAPP [Labrot et al., 2011]. The temperature of the blackbody is measured with n calibrated platinum sensors, where $n = 4$ except for HIRS/4, where $n = 5$. The blackbody temperature is calculated from the mean temperature value from all available internal warm target temperature sensors like this:

$$T_{bb} = \frac{\sum_{i=1}^{n} T_i}{n}. \tag{3.5}$$

The calculated radiance can be converted to a brightness temperature through the inverse Planck's law (inverse of Equation (3.3)).
From the Jet Propulsion Laboratory (JPL) Horizon webpage [NASA, 2022] it is possible to get the angular diameter and the phase angle of the Moon for the exact time and location of the satellite. JPL Horizon provides the angular diameter of the Moon in arcseconds and it is converted to degrees when dividing by the factor 3600. JPL also gives the information if the Moon in trailing or leading the Sun (T/L). Trailing means negative phase angles and leading positive phase angles, while 0° represents full Moon and 180° new Moon, as visualized in Figure 3.1.
The error calculation of the radiance is done through Gaussian error propagation in Equation (3.6).

$$\Delta_{R_{Moon}} = \sqrt{\left(\frac{\partial R_{Moon}}{\partial \overline{X}_{DSV}}\right)^2 \cdot \sigma_{\overline{X}_{DSV}}^2 + \left(\frac{\partial R_{Moon}}{\partial \overline{X}_{Moon}}\right)^2 \cdot \sigma_{\overline{X}_{Moon}}^2 + \left(\frac{\partial R_{Moon}}{\partial \overline{X}_{bb}}\right)^2 \cdot \sigma_{\overline{X}_{bb}}^2} \tag{3.6}$$

The errors of the blackbody radiance R_{bb} and the angular diameter of the Moon, taken from JPL, are negligibly small and therefore not taken into account. The error of the FOV is not a random error but results from a systematic uncertainty and must be considered separately.

$$\frac{\partial R_{Moon}}{\partial \overline{X}_{Moon}} = \frac{FOV^2 \cdot R_{bb}}{\alpha^2 \cdot 0.97 \cdot (\overline{X}_{bb} - \overline{X}_{DSV})}$$

$$\frac{\partial R_{Moon}}{\partial \overline{X}_{DSV}} = -\frac{FOV^2 \cdot R_{bb} \cdot (\overline{X}_{Moon} - \overline{X}_{bb})}{\alpha^2 \cdot 0.97 \cdot (\overline{X}_{bb} - \overline{X}_{DSV})^2} \tag{3.7}$$

$$\frac{\partial R_{Moon}}{\partial \overline{X}_{bb}} = \frac{FOV^2 \cdot R_{bb} \cdot (\overline{X}_{DSV} - \overline{X}_{Moon})}{\alpha^2 \cdot 0.97 \cdot (\overline{X}_{bb} - \overline{X}_{DSV})^2}$$

The relative uncertainty in percent is then calculated through the ratio of the error $\Delta_{R_{Moon}}$ in $\frac{MJy}{sr}$ to the radiance of the Moon R_{Moon} in $\frac{MJy}{sr}$ multiplied with 100.

$$\sigma_{R_{Moon}} = \frac{\Delta_{R_{Moon}}}{R_{Moon}} \cdot 100 \tag{3.8}$$

This relative error for the data set of Moon observations ranges from 0.04% to 19%, depending on the channel and whether the Moon is fully included or not. In general, when the Moon is fully included in the FOV of the selected channel, the relative uncertainty is below 1.5%. The estimation of the systematic error is challenging, because the FOV values differ from the version of HIRS and ground-test data is only available for the very first HIRS/2 and the newest HIRS/4 instruments (see A.3, A.4, A.17 and A.18). In between and especially for HIRS/3, the literature gives very different values from 1.25° [Labrot et al., 2011] to 1.4° for short-wave and 1.3° for long-wave channels [Robel and Graumann, 2014]. As the radiance increases with the square of the FOV of the instrument, the FOV has a huge impact on the calculated radiance value. Therefore, the systematic error estimation for the FOV is predominant in the uncertainty estimation of the radiance and will be evaluated further in Chapter 4.2.5.

4. Results and discussion

The analysis is mainly focused on the water vapour channel 12 at 6.5 μm for HIRS/2 and 6.7 μm for HIRS/3 and HIRS/4.

A total of 123 lunar intrusions were found for which the Moon was fully included in the FOV for channel 12. The complete data set can be downloaded via Zenodo (see Seibert [2022a]).

By directly comparing each observation with a model calculation, the model performance can be tested for dependencies on the Moon's phase angle, the Moon's distance from the Sun, or wavelength dependencies. Furthermore, it is possible to check the stability of the instrument on each satellite by comparing the observations with HIRS against a TPM over time.

4.1. Representativity of measurements

The 123 lunar intrusions were found on 16 different satellites over a large range of phase angles between -90 and +90 degree around full Moon. Since the majority of satellites are equipped with HIRS version 2, most Moon intrusions were also observed with this instrument. Table 4.1 lists how many intrusions were found for each satellite and version of HIRS. For the newer satellites equipped with HIRS/4 only 13 Moon intrusions on 4 satellites could be found. For the Metop satellites it was even harder to find Moon intrusions at all. The main reason for this is most probably the smaller FOV of 0.7°. The angular diameter of the Moon measures $\sim 0.5°$. Therefore its much harder to find observations of the Moon in the DSV, where the Moon is fully included in the FOV (see Figure 2.4).

In addition to the smaller optical FOV, the mission duration plays a major role. Table 2.1 lists the satellites along with the start and end dates. Only two Moon intrusions were found on TIROS-N, which has been in orbit for less than three years. In comparison to that, NOAA-14 has the highest number of Moon observations during calibration procedures, with 24, and has been taken measurements in orbit for more than 12 years.

Table 4.1.: Number of Moon intrusions per satellite and per instrument.

Satellite			Instrument
TIROS-N 2	NOAA-06 5	NOAA-07 7	HIRS/2 67
NOAA-08 4	NOAA-09 5	NOAA-10 10	
NOAA-11 6	NOAA-12 4	NOAA-14 24	
NOAA-15 12	NOAA-16 15	NOAA-17 16	HIRS/3 43
NOAA-18 8	NOAA-19 3	Metop-A/Metop-B 1/1	HIRS/4 13

4.1.1. Brightness temperature dependence on the phase angle

In the following, all Figures are either showing the calculated brightness temperatures in Kelvin or the observed flux divided by the corresponding model prediction versus varying quantities for each satellite equipped with a HIRS sensor. Varying colors indicate different satellites and varying shapes indicate different versions, while the bluish colors with a circle as marker stands for HIRS/2, the yellowish colors with a triangle as marker stands for HIRS/3 and the reddish colors with a square as marker for HIRS/4. Figure 4.1 is the legend for following plots.

● HIRS/2 TIROS-N (1978-1981)	● HIRS/2 NOAA-14 (1994-2007)
● HIRS/2 NOAA-6 (1979-1987)	▼ HIRS/3 NOAA-15 (1998-2021)
● HIRS/2 NOAA-7 (1981-1986)	▼ HIRS/3 NOAA-16 (2000-2014)
● HIRS/2 NOAA-8 (1983-1985)	▼ HIRS/3 NOAA-17 (2002-2013)
● HIRS/2 NOAA-9 (1984-1998)	■ HIRS/4 NOAA-18 (2005-2021)
● HIRS/2 NOAA-10 (1986-2001)	■ HIRS/4 NOAA-19 (2009-2021)
● HIRS/2 NOAA-11 (1988-2004)	■ HIRS/4 Metop-A (2006-2021)
● HIRS/2 NOAA-12 (1991-2007)	■ HIRS/4 Metop-B (2012-2024)

Figure 4.1.: Legend for following plots. Different colors groups and shapes indicate different satellites and versions, while the bluish colors with a circle as marker stands for HIRS/2, the yellowish colors with a triangle as marker stands for HIRS/3 and the reddish colors with a square as marker for HIRS/4.

Figure 4.2 shows the calculated brightness temperatures in Kelvin for all 123 Moon intrusions for channel 12 against the phase angle of the Moon in degrees. The legend for the colors and shapes can be found in Figure 4.1. A 4th order polynomial is fitted to the data and visualized with the solid line in the Figure. In addition, an envelope cosinus is shown with the dashed line, as $315\,\text{K} - 60\,\text{K} \cdot cos(2\pi t)$ with t values reaching from -145°
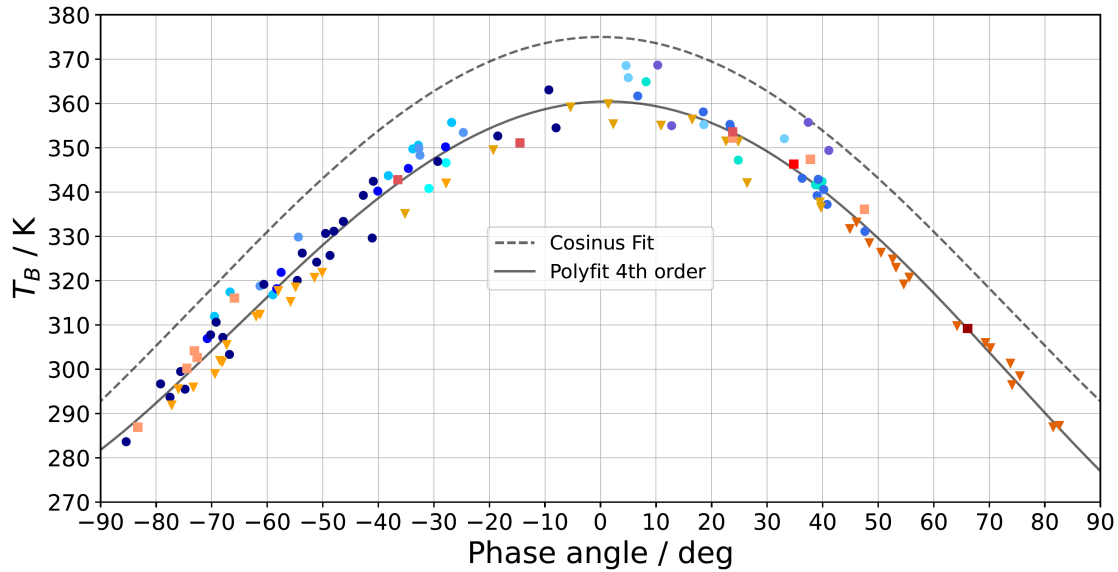
Figure 4.2.: The calculated brightness temperature in Kelvin for all Moon intrusions for channel 12, at a wavelength of 6.5 *μm* for HIRS/2 and 6.7 *μm* for HIRS/3 and HIRS/4, against the phase angle of the Moon in degrees. The different colors indicate different satellites and the shape the version of HIRS, while a circle stands for HIRS/2, the triangle stands for HIRS/3 and the square for HIRS/4. A polynomial 4th order is fitted to the data and visualized with a solid line and an envelope cosinus is shown with the dashes line, as $315\,\mathrm{K} - 60\,\mathrm{K} \cdot cos(2\pi t)$ with t values reaching from -145° to 145°.

to 145°.

56% of the measurements were observed with waning Moon and 43% with waxing Moon. The observation with the largest difference to the full Moon is at an phase angle of -85.4° on NOAA-14. The Moon intrusion with a phase angle closest to full Moon was measured on NOAA-15 with a phase angle of 1.4°. However, with a measured brightness temperature of 359.9 K it is not the observation with the highest brightness temperature. The observation with the highest brightness temperature of 368.5 K for channel 12 is on NOAA-08 with a phase angle of 4.6°.

Overall, the Moon observations show good agreement across all versions of HIRS. As an example, three different Moon intrusions, each with different HIRS version, are selected at a similar phase angle. HIRS/2 on NOAA-10 measured on 7th November 1987 at a phase angle of 23.4° a brightness temperature of 354.7 ± 0.1 K, HIRS/3 on NOAA-15 measured on 8th March 2004 at a phase angle of 22.6° a brightness temperature of 351.5 ± 0.2 K and HIRS/4 on NOAA-19 measured on 2nd November 2020 at a phase angle of 23.8° a brightness temperature of 355.3 ± 0.1 K. The errors are relative small, because they only result from the count deviations during the space views (see Equation 3.6).

4.2. Comparison of observations with the thermal physical model

The thermo-physical model (TPM) from Müller et al. [2021] is used for a comparison of the measurement results. As described in 2.2 the model output for the radiance of the Moon is provided in Jansky. To make it comparable with the HIRS observations it is converted with Equation (2.3) to a radiance in $\frac{\text{MJy}}{\text{sr}}$. The calculations are conducted for the exact time and position of the satellite with accurate distances to the Moon and the Sun.

4.2.1. Dependence on the phase angle
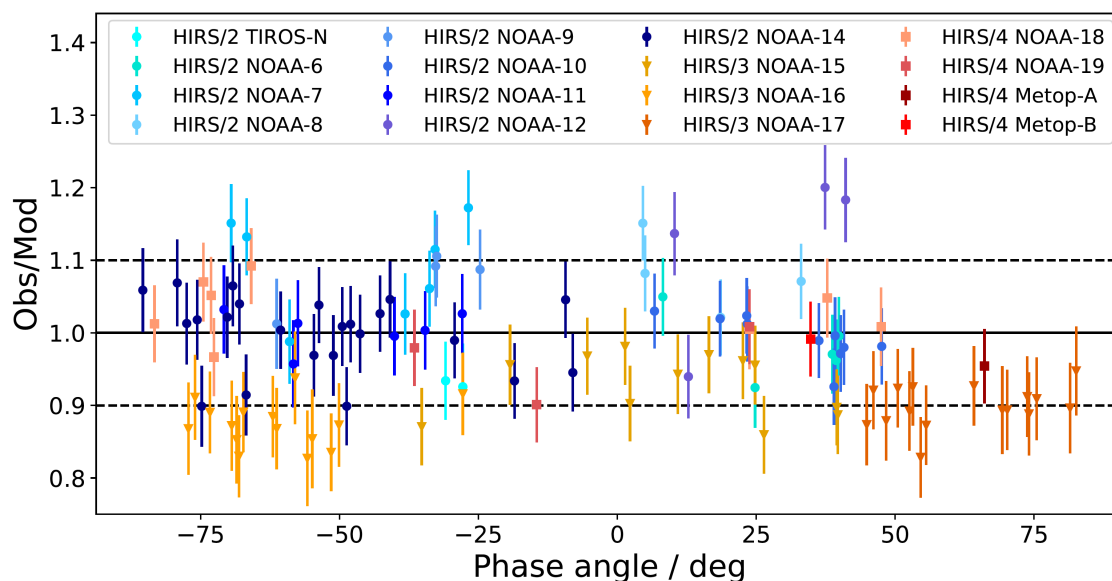
Figure 4.3.: Moon observations with HIRS divided by the TPM calculations in dependence of the phase angle of the Moon for channel 12, at a wavelength of 6.5 μm for HIRS/2 and 6.7 μm for HIRS/3 and HIRS/4. The different colors indicate different satellites and the shape the version of HIRS, while a circle stands for HIRS/2, the triangle stands for HIRS/3 and the square for HIRS/4. The dashed horizontal lines represent the +/-10% difference of the observations and the model. The error bars represent the quadratic addition of the relative errors.

Figure 4.3 shows the observations divided by the model against the phase angle of the Moon for channel 12. The colors and shapes indicate the satellite and the version of HIRS. The dashed horizontal lines represent the +/-10% difference of the observations and the model. The error bars represent the quadratic addition of the relative errors. The error bars result from the quadratic addition of the errors from measurement and model calculations. The calculated relative error for the HIRS measurements are from Equation (3.8), and the relative error for the model calculations is assumed to be 5%. If model and ob-

servation were exactly the same, all points would lie on $y = 1.0$. The points are equally distributed around 1 in the +/-10% range. Some observations on NOAA-07, NOAA-08 and NOAA-12 are more than 10% above the model calculations. Taking the average and the standard deviation of all observations divided by the model predictions of channel 12 for each version of HIRS results in 1.023 ± 0.069 for HIRS/2, 0.899 ± 0.040 for HIRS/3 and 1.007 ± 0.049 for HIRS/4. The observations of Channel 12 with HIRS/2 are on average 2.3 percent above the model predictions and have a standard deviation of 6.9%. Since HIRS/2 is the instrument with the most satellites and also observations, a larger scatter is also to be expected. It is striking that the mean fluxes of HIRS/3 are systematically below the model calculations by 10% with a standard deviation of 4%. Thus, it can be assumed that there is a systematic error in the data for satellites equipped with HIRS/3. In Section 4.2.5 it will be further investigated, if a wrong estimated FOV might be the reason for these larger differences. HIRS/4 is on average only very slightly above the model calculations with 0.7% and has a standard deviation of 4.9%.

In the publication from Müller et al. [2021] already 22 Moon observations with HIRS were compared with the TPM, with the observations serving as validation for the model. it was not clear how the model performance would be near full Moon. It was unclear how the model performance would be near full Moon, because the 22 Moon observations were observed at phase angles more than 15° away from full Moon. The model was developed for calculations of asteroids and includes a function for considering the beaming effect (see Equation (2.1)). However, it was not clear whether the model also reproduces the beaming effect well enough at full Moon. With the complete data set of Moon observations with HIRS, I can confirm that the model is representative over the phase angle range from -85° to +85°, because no phase angle dependent deviation could be detected.

4.2.2. Dependence on the distance to the Sun

The brightness temperature of the Moon varies with the distance between the Moon and the Sun. Figure 4.4 shows the calculated brightness temperature in Kelvin for all Moon intrusions for channel 12, at a wavelength of 6.5 μm for HIRS/2 and 6.7 μm for HIRS/3 and HIRS/4, against the phase angle of the Moon in degrees. The legend for the colors and shapes can be found in Figure 4.1. In comparison to the measurements, model calculations for three different distances of the Moon to the Sun are plotted. The solid line represents the nearest possible distance of the Moon to the Sun, where the Earth is at Perihelion and the Moon at Apogee with a heliocentric distance of $r = 0.9806$ au. The dashed line is the middle position at a distance of $r = 1.0$ au and the dotted line the furthest distance of the Moon to the Sun with Earth at Aphelion and the Moon at Apogee at $r = 1.0194$ au. Figure 4.4 visualises that the model predictions are asymmetrical around full Moon, because the TPM considers thermal inertia. The Moon rock at waning Moon on the dark half of the Moon is still heated in a few millimeter of the surface and is there-

fore measured still somewhat warmer than at waxing Moon. This effect is even more prominent at longer wavelengths, because the thermal radiation is coming from deeper layers in the rock. The effect of thermal inertia is assumed to be stronger, when the Moon has a small distance to the Sun. With the graphical representation in Figure 4.4 the information of the heliocentric distance of each observation is not obvious and we can not interpret the brightness temperatures properly without this information.
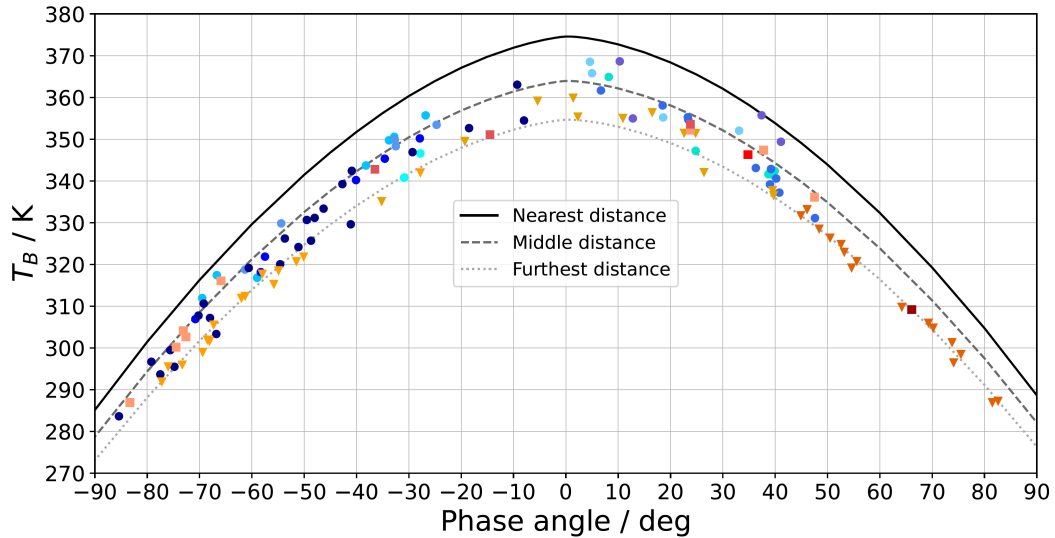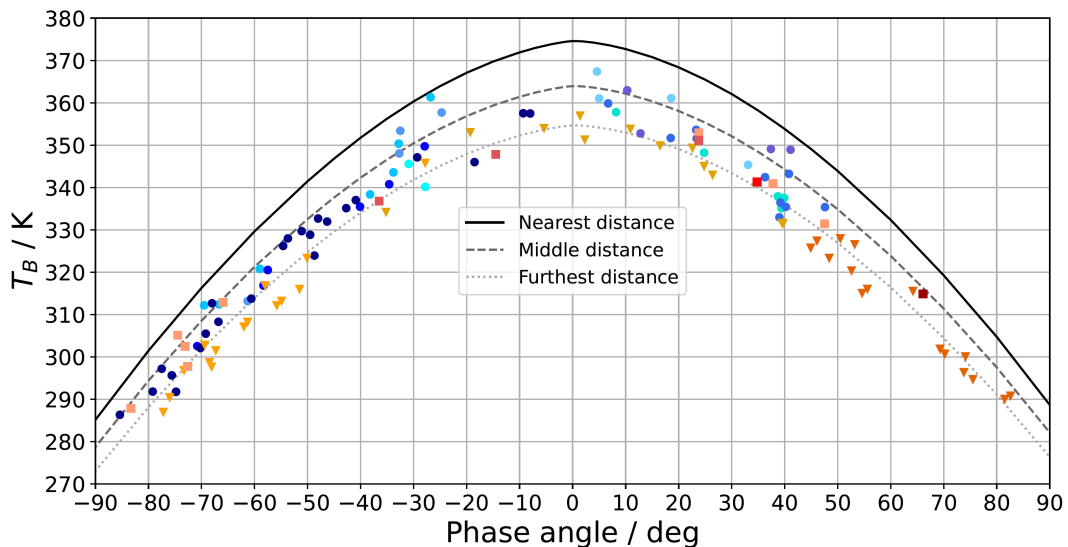
Figure 4.4.: The calculated brightness temperature in Kelvin for all Moon intrusions for channel 12 against the phase angle of the Moon in degree. In comparison to the measurements, model calculations for three different distances of the Moon to the Sun are plotted. The solid line represents the nearest distance of the Moon to the Sun with a heliocentric distance of 0.9806 au, the dashed line the middle position at a distance of 1.0 au and the dotted line the furthest distance to the Sun at 1.0194 au.

Figure 4.5.: The calculated brightness temperature in Kelvin for all Moon intrusions for channel 12 against the phase angle of the Moon in degree corrected for the distance to the Sun. In comparison to the measurements, model calculations for three different distances of the Moon to the Sun are plotted. The solid line represents the nearest distance of the Moon to the Sun with a heliocentric distance of 0.9806 au, the dashed line the middle position at a distance of 1.0 au and the dotted line the furthest distance to the Sun at 1.0194 au.

That is the reason why a correction of the distance to the Sun was implemented in Figure 4.5. The calculation of the correction was done with this formula:

$$R_{Moon,corr} = \left(1 + \frac{(r - r_{mid}) \cdot 7.7246}{r_{mid}}\right) \cdot R_{Moon}, \qquad (4.1)$$

while $r_{mid} = 1.0$ au. The factor that is multiplied is estimated from the flux change of the model calculations for the different distances and assuming that the flux change is linear with distance. The difference of the flux at the middle distance to the flux at nearest distance is 15%, which explains the factor multiplied in Equation 4.1. Figure 4.5 shows the observations corrected for the middle distance of 1 au. With this correction all observations should ideally lie on the dashed line which represents the middle distance at $r = 1.0$ au. Unfortunately, this is not the case, but one must remember that most of the data extremely below the dashed line are observations recorded with the instrument HIRS/3. In chapter 4.2.5 it will be further investigated whether the FOV of HIRS/3 is not 1.3°.

When comparing the observed fluxes directly with the model calculations, the correction for the distance to the Sun is no longer needed, because the model considers the exact heliocentric distance already. Figure 4.6 shows the observations divided by the model for channel 12 against the heliocentric distance of the Moon to our Sun. The colors and shapes indicate the satellite and the version of HIRS. The dashed horizontal lines represent the +/-10% difference of the observations and the model. The error bars represent the quadratic addition of the relative errors. The calculated error for the HIRS measurements from Equation (3.8) and a relative error of 5% for the model calculations. From Figure 4.6 it can be deduced that most observations of the Moon are closer than the mean distance of 1 au to the Sun. Here again, it is obvious that all observations with HIRS version 3 are smaller than the model calculations. In general, no distance dependent shift is visible, thus the model is performing well for all heliocentric distances.
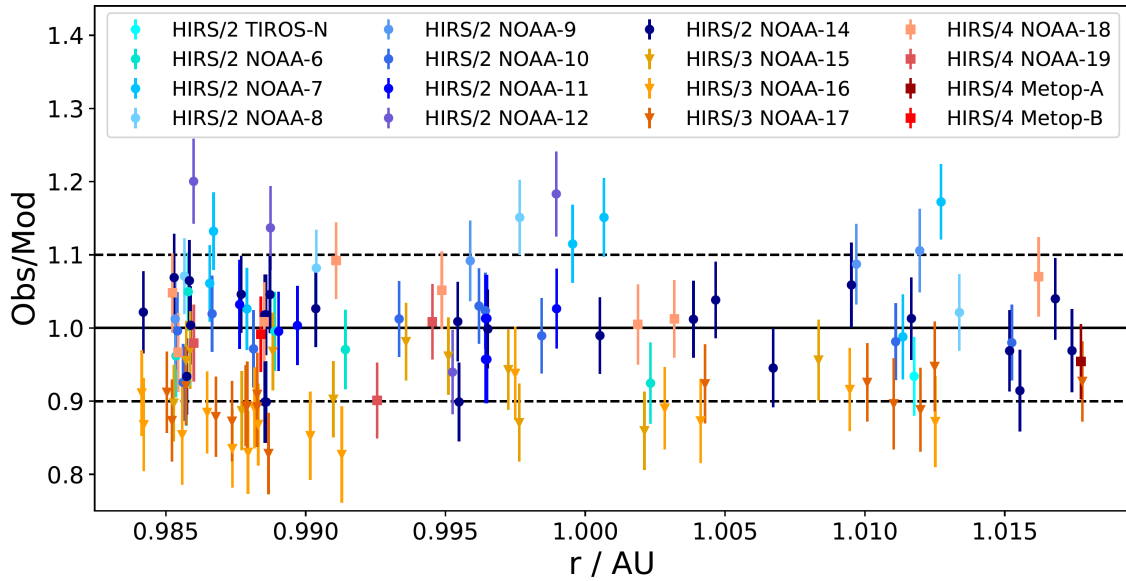
Figure 4.6.: Moon observations with HIRS divided by the TPM calculations in dependence of the distance to the Sun for channel 12, at a wavelength of 6.5 μm for HIRS/2 and 6.7 μm for HIRS/3 and HIRS/4. The different colors indicate different satellites and the shape the version of HIRS, while a circle stands for HIRS/2, the triangle stands for HIRS/3 and the square for HIRS/4. The dashed horizontal lines represent the +/-10% difference of the observations and the model. The error bars represent the quadratic addition of the relative errors.

4.2.3. Stability of HIRS

When comparing the HIRS measurements with the TPM it is possible to analyze the stability of the instrument, because the model definitely stayed constant over the time. Figure 4.7 shows the observations with HIRS divided by the TPM in dependence of the time for channel 12. The different colors indicate different satellites and the shape the version of HIRS, while a circle stands for HIRS/2, the triangle stands for HIRS/3 and the square for HIRS/4. The dashed horizontal lines represent the +/-10% difference of the observations and the model. The error bars represent the quadratic addition of the relative errors. The time series starts with the observations on TIROS-N in 1979 and ends with observations on NOAA-19 in 2021. Most of the observations are lying within the +/-10% difference to the model. Six out of seven observations on NOAA-07 are above the model values, whereof four observations are more than 10% higher than the model calculations. Even higher radiances are observed on NOAA-12, while one observation is below the model calculations. For the first satellites equipped with HIRS/2, namely TIROS-N, NOAA-06, NOAA-07, NOAA-08 and NOAA-09, a drift to higher measured flux values is visible with increasing time. So, for these satellites a correction for the time-dependent drift should be conducted. Satellites from NOAA-10 onwards seem to be stabilized showing no drift in time. Again, it is obvious that all observations con-

ducted with the instrument HIRS version 3 are systematic below the model calculations. A correction to a greater than presumed value of the optical FOV would increase the flux values, please refer to chapter 4.2.5 for more details.
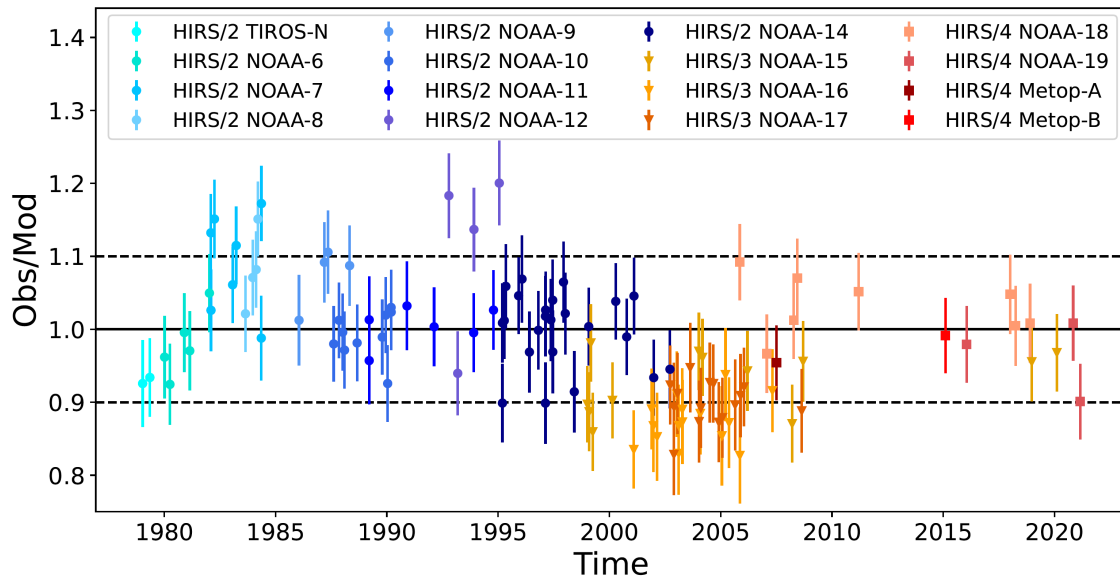
Figure 4.7.: Time series of Moon observations with HIRS divided by the TPM calculations for channel 12, at a wavelength of 6.5 μm for HIRS/2 and 6.7 μm for HIRS/3 and HIRS/4. The different colors indicate different satellites and the shape the version of HIRS, while a circle stands for HIRS/2, the triangle stands for HIRS/3 and the square for HIRS/4. The dashed horizontal lines represent the +/-10% difference of the observations and the model. The error bars represent the quadratic addition of the relative errors.

4.2.4. **Dependence on the wavelength**

In addition to phase angle and heliocentric distance, the Moon's brightness temperature also varies depending on what wavelength we are looking at. As described in Chapter 2.1 the instrument HIRS has 19 IR channels resulting from two optical paths in 12 long-wave and 7 short-wave channels. The center frequencies for channel 10 and channel 12 changed with the version of HIRS. When comparing the observations of the Moon directly with the TPM it is possible to analyze wavelength-dependent characteristics of the instrument as well as the performance of the model.

In the following, all figures show the observation divided by the model calculations against the wavelength in μm. Each marker is another channel and each color a different Moon observation. The dashed lines represent the +/-10% difference between observation and model. Three satellites are selected to be discussed in this section, while the plots for all other satellites can be found in Appendix A.2. Channel 1 at 14.96 μm is excluded in most cases because it shows high noise. In all versions of HIRS, channel 1 has by far the largest noise equivalent delta radiance (see Table A.1 and Table A.2).

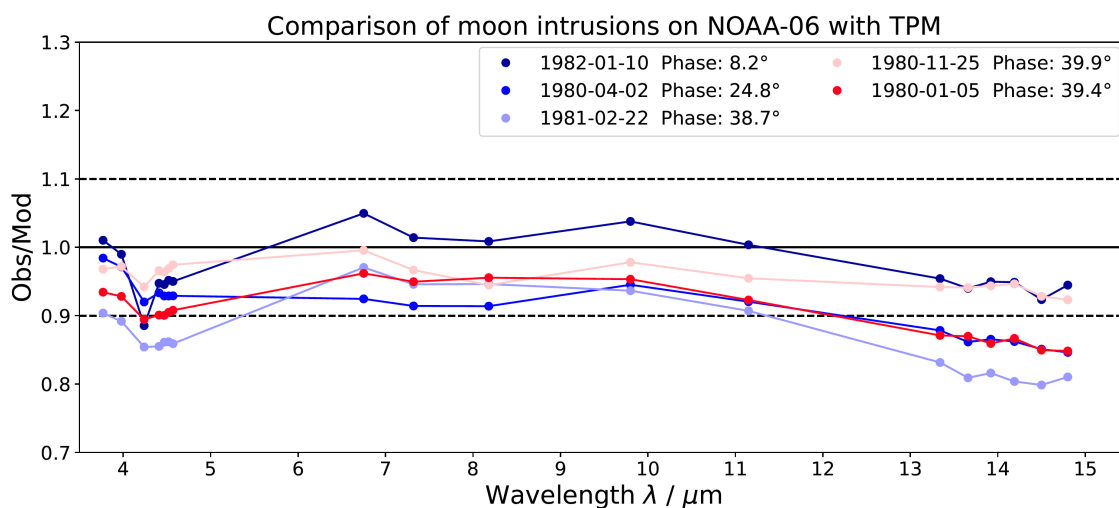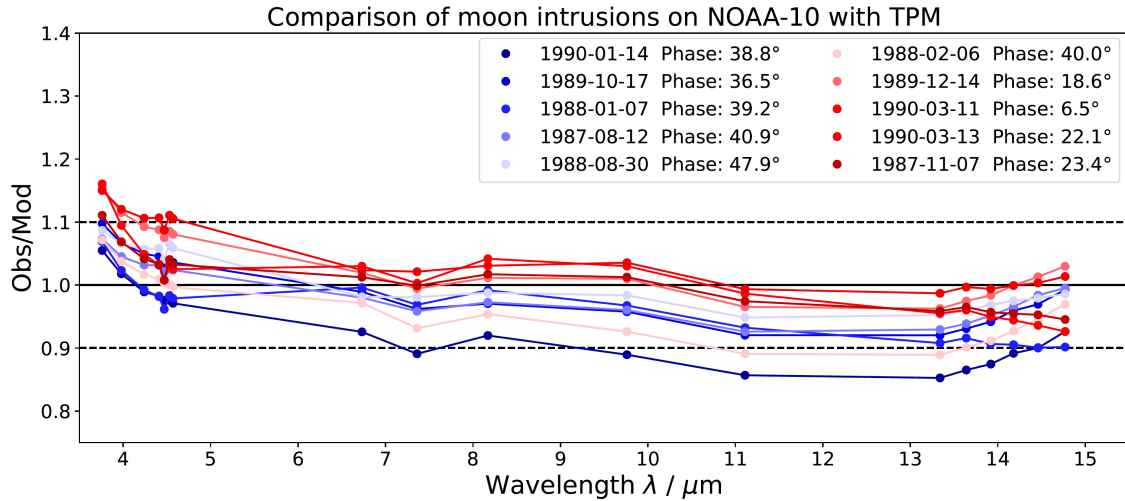Figure 4.8 shows the comparison of the Moon intrusions on NOAA-14. NOAA-14 is
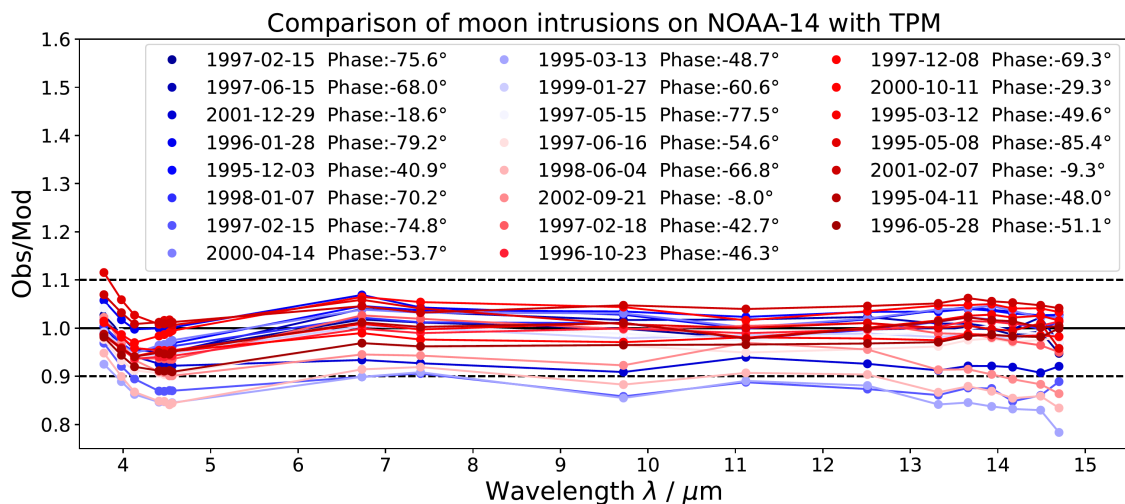
Figure 4.8.: Moon observations with HIRS divided by the TPM calculations in dependence of the wavelength on NOAA-14. Each color is a different Moon observation. The dashed horizontal lines represent the +/-10% difference of the observations and the model.

selected, because most lunar observations with HIRS/2I on NOAA-14 with a total of 24 Moon intrusions. 19 out of 24 Moon intrusions are lying completely inside the +/-10% difference range around 1.0 and show the same principal curve characteristic over the whole wavelength range. The short-wave channels 13-19, which are between 3.78 and 4.56 μm show strongly increasing values for decreasing wavelength. Unknown calibration errors of the HIRS detectors in this regime cannot be excluded entirely, but it is more likely that the discrepancies are related to the model calculations. The transition region

between reflected sunlight and thermal emission is very sensitive to global surface scattering and emissivity properties which are not well known. In addition, the reflected light calculations are not well tested (seen below about 4.5 μm) and the implementation of surface roughness in the TPM code has a noticeable influence of the predicted short-wavelength radiances. That is why a comparison at these wavelengths is for qualitative purposes only and can not provide a quantitative characterization.

The principal curve characteristic is more or less the same for all observations, but five observations are systematically below the other observations. Especially in the longer wavelength range from 9 to 15 μm they show a varying curve structure. For all observations it was assumed that the Moon was inside the FOV, but the Moon may not be fully included in all observations. When the Moon is not 100% in the FOV, the measured flux is slightly to low and that is why some observations are below the model calculations.

Figure 4.9.: Moon observations with HIRS divided by the TPM calculations in dependence of the wavelength on NOAA-06. Each color is a different Moon observation. The dashed horizontal lines represent the +/-10% difference of the observations and the model.

Figure 4.9 shows the comparison with NOAA-06, which counts five Moon observations at different phase angles. The principal shape along the wavelength range is very similar for all observations. The channels in the long-wave range between 12 and 15 μm and the short-wave range between 3.5 and 5 μm are systematically below the model, while the middle range between 6 and 11 μm shows higher observed flux and lies exactly between the +/-10% difference range between observation and model. The highest fluxes are noticeable for either channel 12 at 6.75 μm or for channel 9 at 9.80 μm for all observations. In comparison to the HIRS/2I on NOAA-14, where channel 10 has its center wavelength at 12.51 μm, HIRS/2 on NOAA-06 has the center wavelength at 8.18 μm. This is of particular interest, because this wavelength is near the location of the mid-infrared emissivity

Figure 4.10.: Moon observations with HIRS divided by the TPM calculations in dependence of the wavelength on NOAA-10. Each color is a different Moon observation. The dashed horizontal lines represent the +/-10% difference of the observations and the model.

maximum, the so-called Christiansen Feature, in the spectrum of the Moon.

A striking feature is present at channel 17 at 4.24 μm for all observations with NOAA-06. Since this drop occurs in observations with very different phase angles, it is assumed that this is no feature resulting from the Moon spectrum. Even if the model is not representative in this wavelength range, this sudden drop was not visible in the observations on NOAA-14 (see Figure 4.8). This is why it can be assumed, that there is a difference in the instrument causing this sudden drop in flux.

Observations taken with NOAA-10 show the same effect of a sudden drop, but instead of channel 17 the drop is present for channel 15 at 4.47 μm, see Figure 4.10. This drop is clearly visible in all observations at different phase angles, but smaller than for channel 17 on NOAA-06. The principal curvature along the wavelengths stays the same for the observations on NOAA-10, except for two Moon observations where the values between 13 and 15 μm are slightly going down, where as for all other observations the values are going up. A local minimum for channel 11 at 7.36 μm is visible in all observations, which was not visible for the observations on NOAA-14 and NOAA-06.

The exact reason for the sudden drop in measured flux versus model flux can not be clarified. Probably channel 17 on NOAA-06 and channel 15 as well as channel 11 on NOAA-10 have a different pointing than the other channels. If the pointing direction of the channels are different, it is possible that the Moon was fully included in the FOV of one channel and not fully included for another channel. A pointing analysis can be performed with the observations of the Moon in flight, but was not performed in this work. Further investigations with a detailed pointing analysis will help to clarify this instrumentation effect.

4.2.5. Field of view estimation

In addition to all the dependencies of the brightness temperature variations analyzed above, such as phase angle, heliocentric distance and wavelength, it is also possible to analyze which FOV size is correct when comparing to the model calculations. The calculation of the radiance of the Moon includes the size of the FOV squared in Equation 3.2. Therefore, the size of the FOV has a significant impact on the result of the calculated radiance.

Many different values for the size of the FOV are given in the literature, and for some satellites it is not clear which source is assumed to be correct. In the previous results one has seen systematic deviations from the model calculations for some satellites, e.g. all satellites with HIRS/3. So in comparison to the model calculations it is possible to check which FOV size is correct.

In the following, all Figures show the radiance from the observation divided by the model calculations against the wavelength in μm. The black dashed horizontal lines represent the +/-10% difference between observation and model. Each color is a different Moon observation and the markers indicate two different calculations, which were performed for each observation. A first order polynomial was fitted to each calculation to check which FOV size is assumed to be correct.

A FOV value is usually specified for the entire instrument, which is $(1.4 \pm 0.03)°$ according to Burgdorf et al. [2020] but $1.25°$ regarding Labrot et al. [2011] and $1.25°$ regarding Koenig [1980] for HIRS/2. In the technical report from Koenig et. al. [1979], however, ground tests are published for the first two satellites equipped with HIRS/2. These tests show that the size of the FOV depends on the wavelength with ranging values from $1.16°$ to values of $1.24°$ for different channels. The measurements of the FOV for TIROS-N are listed in Table A.3 and for NOAA-06 in Table A.4. Apparently for some channels no ground test data is available. In these cases it was assumed that the values of the adjacent channels are also correct for the respective channel. For NOAA-06 values for channel 1 and channel 2 are missing, so the measured value from channel 3 of $1.16°$ was assumed to be correct for channel 1 and 2 as well. For TIROS-N values for channel 1 and channel 2 are missing, so the measured value for channel 3 of $1.18°$ was assumed to be correct. Also, channel 12 was missing so the value for channel 11 of $1.20°$ was assumed to be correct. Channels 14-17 were missing, so the value of channel 18, which was measured to be $1.23°$, was assumed to be correct for the channels 14, 15, 16 and 17. To check which size of the FOV is correct, the Moon observations on this two satellites were calculated once with the values of the ground tests and in comparison with the FOV of $1.2°$ for all channels.

Figure 4.11 and Figure 4.12 are showing the Moon observations with TIROS-N and NOAA-06 in comparison to the model calculations against the wavelength for two different assumptions for the size of the FOV of the instrument. The circles represents the calculations assuming for all channels the same FOV size of $1.2°$, while the triangles show the

calculations for the wavelength-dependent FOV values from the ground tests. The solid lines are first order polynomial fits to the wavelength-dependent FOV size from ground test, while the dashed lines represent first order polynomial fits to the calculations with a FOV size of 1.2° for all channels. For all observations on both satellites the solid lines are showing less to no slope in comparison to the dashed lines. This means the wavelength-dependent FOV sizes are fitting better to the calculations, when comparing to the model calculations.
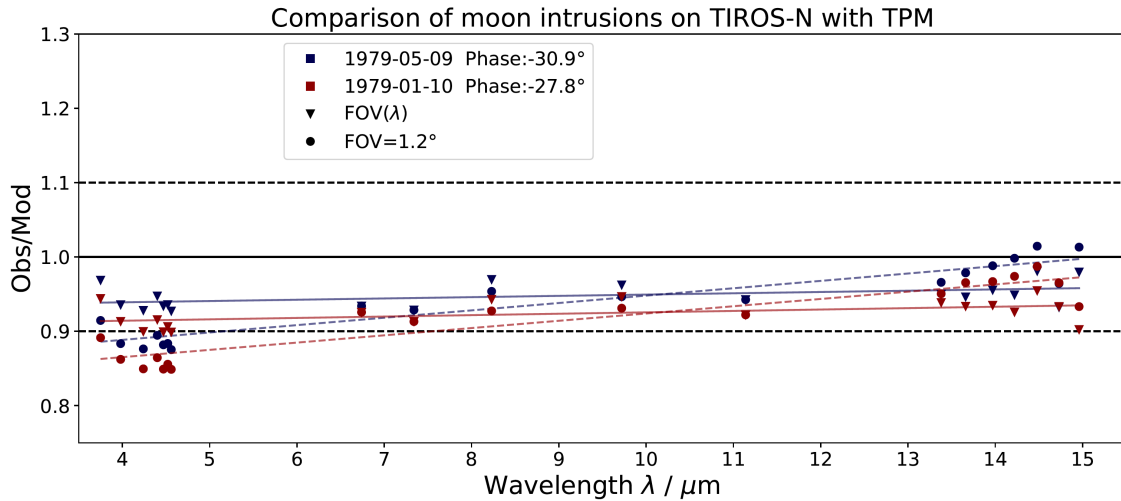
Figure 4.11.: Moon observations with HIRS divided by the TPM calculations in dependence of the wavelength on TIROS-N for two different FOV sizes. Each color is a different Moon observation. The dashed horizontal lines in black represent the +/-10% difference of the observations and the model.

In Section 4.2.3 the measurements with HIRS/2 on NOAA-12 show extremely high observed flux in the comparison to the corresponding model predictions. Lower values compared to the model can easily be explained by the fact that the Moon was possibly not 100% in the FOV, but much higher values are most likely due to the fact that the FOV was assumed to be larger than it actually is. Using the same method as for TIROS-N and NOAA-06, two calculations with different FOV sizes were performed. One calculation used the value of 1.4°, which was previously assumed to be correct for the FOV for all HIRS/2. The second calculation was made for 10% lower radiances, which means a 5% lower, or 1.33°, FOV. The standard deviation from all HIRS/2 values was calculated in Section 4.2.1 to be 6.9%, so the error of the FOV for NOAA-12 results in 0.09°. The analysis yield to a FOV size of $(1.33 \pm 0.09)°$ for the long-wave channels for HIRS/2 on NOAA-12. As already discussed in Section 4.2.3, the values from the satellites equipped with HIRS/3 lie systematically below the model calculation by around 10%. That is why I assume, that the FOV of the instrument HIRS/3 is higher than the expected value from Burgdorf et al. [2020] of 1.3°. A 9% higher flux results in 4.4% higher FOV, which is 1.36° instead of the previously expected size of 1.3°. The standard deviation from all HIRS/3
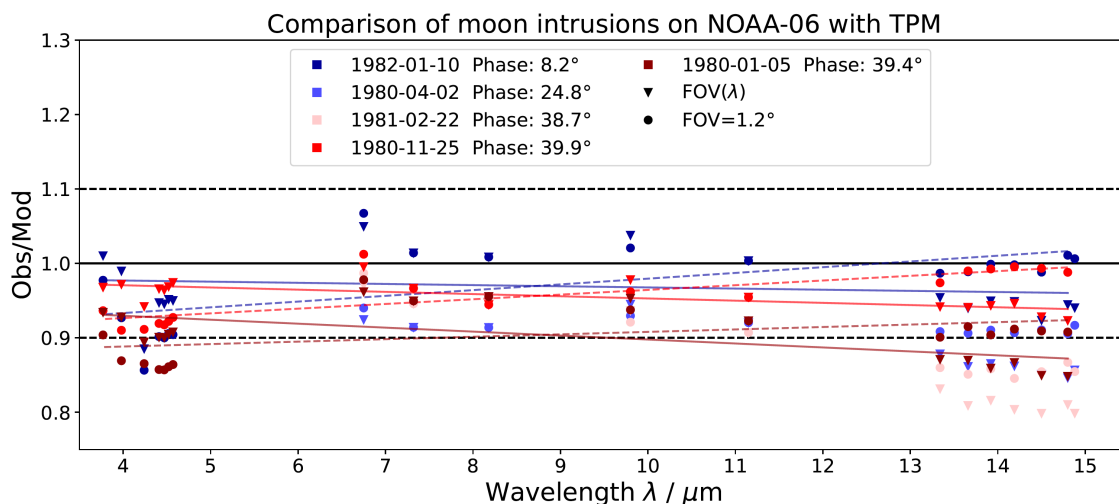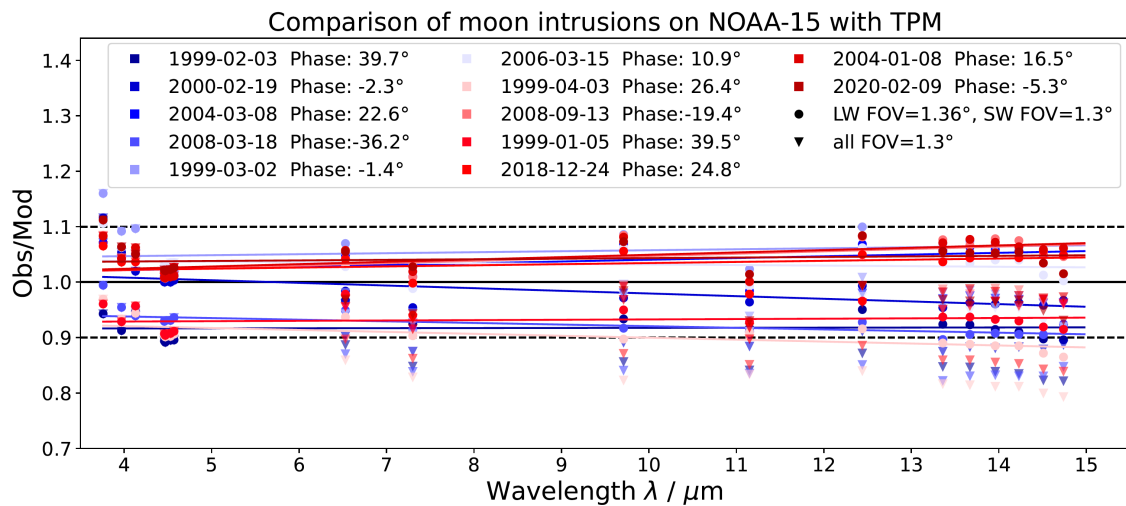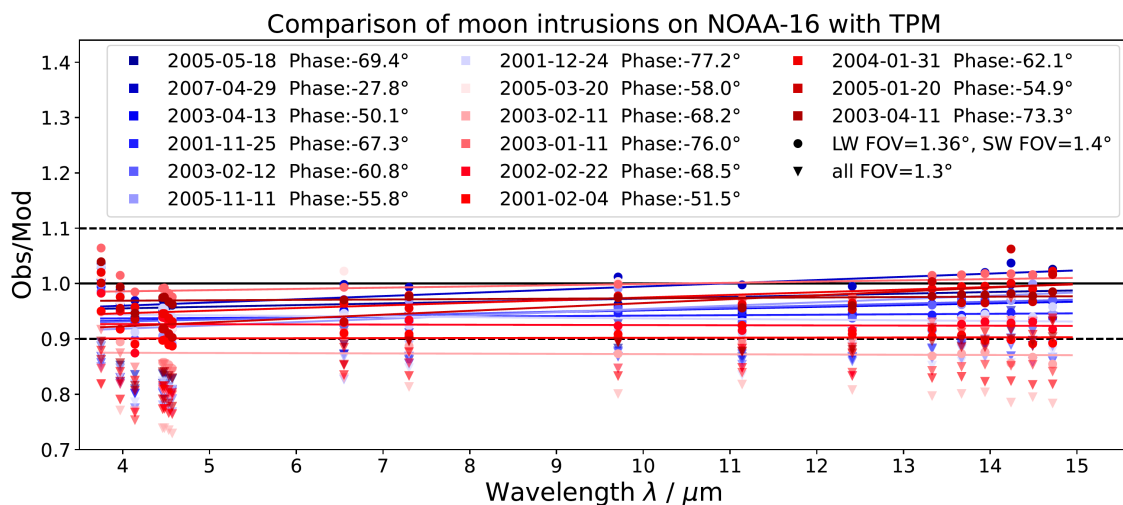
Figure 4.12.: Moon observations with HIRS divided by the TPM calculations in depen-
             dence of the wavelength on NOAA-06 for two different FOV sizes. Each
             color is a different Moon observation. The dashed horizontal lines in black
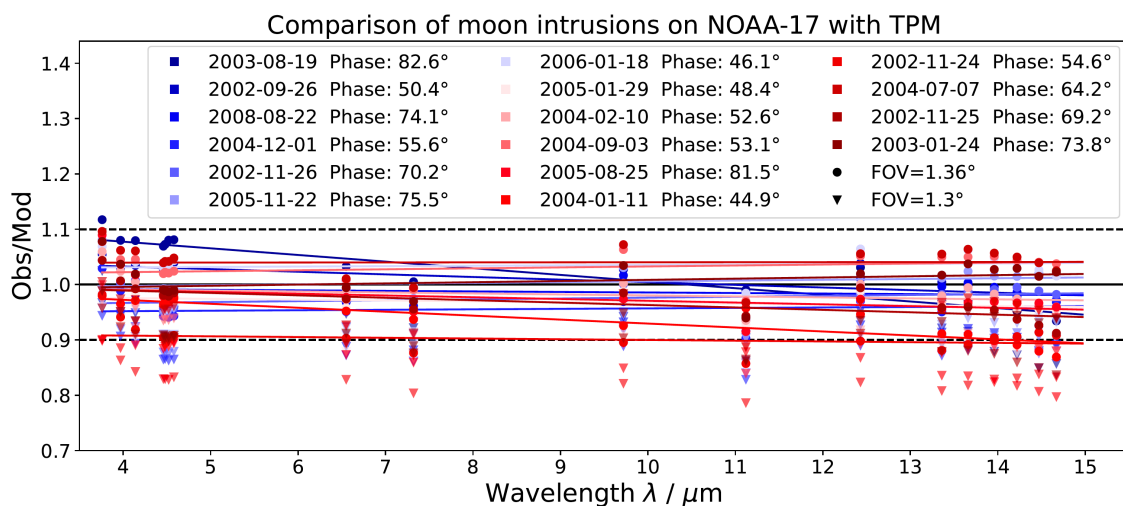   represent the +/-10% difference of the observations and the model.

values was calculated in Section 4.2.1 to be 4%, so the error of the FOV for HIRS/3 re-
sults in 0.05°. Figure 4.13, Figure 4.14 and Figure 4.15 are showing the Moon intrusions
on NOAA-15, NOAA-16 and NOAA-17 respectively. The triangles represent the calcu-
lations with a FOV of 1.3° for all channels. The dashed lines are showing the first order
polynomial fit to this data. The new assumed values are represented by circles and the
corresponding polynomial fit of the first order is shown with the solid line.

For NOAA-15 in Figure 4.13 the measurements in the short-wave regime seem to fit re-
ally good in comparison to the model calculations already, so it was assumed that the
short-wave and long-wave channels are having different FOV sizes. In principal, this
would make sense since the beam paths through the relevant detector are different and
the KLM User's Guide states that the instantaneous FOV for each channel on HIRS/3 is
approximately 1.4° in the short-wave IR and 1.3° in the long-wave IR [Robel and Grau-
mann, 2014]. But instead of a bigger FOV for the short-wave, it seems to be the other way
around. The values are fitting better in comparison to the model for a FOV of 1.36° in the
long-wave and a FOV of 1.3° in the short-wave regime.

For the sake of clarity, the polynomial fits for the original data set are omitted in Fig-
ures 4.14 and 4.15. For HIRS/3 on NOAA-16 and NOAA-17 it appears that the sizes of
the FOV of the short-wave channels are different than on NOAA-15. All observations
on NOAA-17 with a FOV size of 1.3° in Figure 4.15 are too low in comparison to the
model, so the new calculations were performed assuming all channels are having a FOV
of 1.36°, which fits much better overall. For the observations on NOAA-16 in Figure 4.14
the short-wave channels of the original data set are further below the model than the
long-wave channels. So, the radiance values of the short-wave channels were multiplied

by the factor of 1.16, which represents 7.7% higher flux and a FOV size of 1.4°. The following conclusions are made for the long-wave channels only, because the model might not be representative in the short-wave regime.

To conclude the FOV estimation, the ground test data of TIROS-N and NOAA-06 are assumed to be correct. This is in accordance with the technical report from Koenig et. al. [1979], where a coating layer on the optics is causing a wavelength-dependent difference for each channel. For NOAA-12 the estimated FOV is 5% higher than the values for other HIRS/2 with a value of $(1.33 \pm 0.09)°$ for the long-wave channels. The FOV of HIRS/3 is estimated to be $(1.36 \pm 0.05)°$ instead of 1.3°, which results in 9% higher radiance values. Figure 4.16 shows the time series of all satellites equipped with HIRS with corrected FOV values for NOAA-12, NOAA-15, NOAA-16 and NOAA-17. This shows that we have stable instruments from 1990 onwards and that there is a 30-year period of HIRS data that shows no drift over time. This time series is very valuable for climate research.

Figure 4.13.: Moon observations with HIRS divided by the TPM calculations in dependence of the wavelength on NOAA-15 for two different FOV sizes. Each color is a different Moon observation. The dashed horizontal lines in black represent the +/-10% difference of the observations and the model.

Figure 4.14.: Moon observations with HIRS divided by the TPM calculations in dependence of the wavelength on NOAA-16 for two different FOV sizes. Each color is a different Moon observation. The dashed horizontal lines in black represent the +/-10% difference of the observations and the model.

Figure 4.15.: Moon observations with HIRS divided by the TPM calculations in dependence of the wavelength on NOAA-17 for two different FOV sizes. Each color is a different Moon observation. The dashed horizontal lines in black represent the +/-10% difference of the observations and the model.
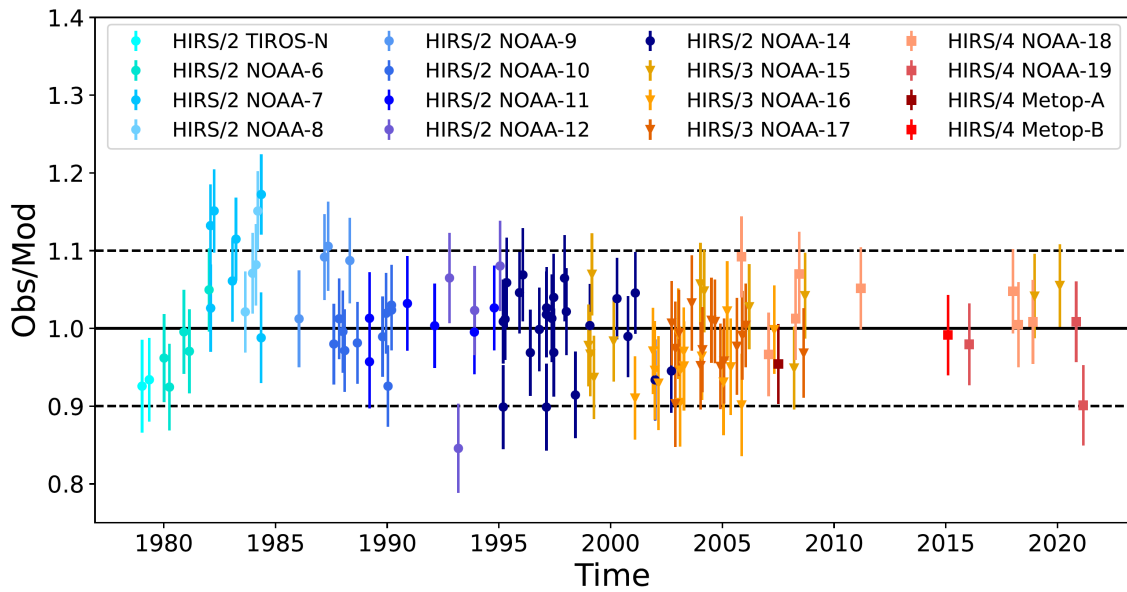
Figure 4.16.: Time series of Moon observations with HIRS divided by the TPM calculations for channel 12 corrected for FOV values on NOAA-12, NOAA-15, NOAA-16 and NOAA-17. Channel 12 is at a wavelength of 6.5 μm for HIRS/2 and 6.7 μm for HIRS/3 and HIRS/4. The different colors indicate different satellites and the shape the version of HIRS, while a circle stands for HIRS/2, the triangle stands for HIRS/3 and the square for HIRS/4. The dashed horizontal lines represent the +/-10% difference of the observations and the model. The error bars represent the quadratic addition of the relative errors.

5. Conclusions and outlook

In this thesis, I set up filter criteria to find and select possible Moon intrusions in the DSV of the HIRS instrument. A total of 123 Moon observations with HIRS on 16 different satellites were analyzed with the focus on channel 12, which is important for the climate variable UTH. The disk-integrated flux values are covering a phase angle range from -85.4° (waxing Moon) to +82.6° (waning Moon), taken between 1979 and 2020. The calculated brightness temperatures are representative for all versions of HIRS. The calibrated time-series of HIRS shows that the older satellites undergo a drift in time to higher radiances compared to the model calculations of the Moon. No time drift was visible from 1990 onward, because newer satellites are more stable. With the comparison to the model the change of the central wavelength of channel 12 from 6.5 to 6.7 μm does not result in a discontinuity in the time-series, because the model calculations also consider the wavelength shift. This means that a 30 year period of calibrated HIRS data exists, which is very valuable for climate research.

It was possible to validate the model, which was not tested for phase angles near full Moon before. I found, that the TPM is representative over the phase angle range from -85° to +85° and for every possible heliocentric distance to the Sun. In principle, no wavelength dependency could be detected, but the short-wave regime below about 5 μm showed observed fluxes which deviate from the model predictions (in some cases outside the +/-10% corridor). Unknown calibration errors of the HIRS detectors in this regime cannot be excluded entirely, but it is more likely that the discrepancies are related to the model calculations. The transition region between reflected sunlight and thermal emission is very sensitive to global surface scattering and emissivity properties, which are not well known. In addition, the reflected light calculations are not well tested (seen below about 4.5 μm) and the implementation of surface roughness in the TPM code has a noticeable influence of the predicted short-wavelength radiances. Nevertheless, it was possible to detect satellite specific anomalies, which are most likely resulting from different pointing directions of the channels. Since the examination of pointing directions of all channels is time-consuming due to differences for each satellite, it would be worthwhile to investigate a proper pointing analysis in a future work.

HIRS/3 showed significant lower radiances than all other observations. By comparing with the TPM it was possible to identify the systematic error and correct the wrong estimated FOV sizes on several satellites. Thereby, I solved the confusion about the different sizes of FOV with changing satellites and versions of HIRS. For newer HIRS/2 the FOV was assumed to be 1.4° for all channels, but the ground-test data of TIROS-N and

NOAA-06 by Koenig et. al. [1979] showing wavelength-dependent values between 1.16°
and 1.24°. I confirm that the ground test data for the first two satellites with HIRS/2 are
correct by comparing the observations of the Moon with the TPM. I claim, that the FOV
is $(1.33 \pm 0.09)°$ for the long-wave channels of NOAA-12, which is smaller than the value
of 1.4° for other satellites with HIRS/2. Due to an error in production it may well be
that a single satellite shows a different size for the FOV of the same instrument version.
Table 2.1 shows that NOAA-12, which is also named NOAA-D, already was under con-
struction after NOAA-7 launched, but was launched after NOAA-11. This could be an
indication that there were problems with NOAA-12 in manufacturing, but there are no
sources in the literature to prove this conclusion. Further, the FOV of HIRS/3 is estimated
to be $(1.36 \pm 0.05)°$ instead of 1.3°.

Chen et al. [2020] developed an improved Moon intrusion detection algorithm on Cross-
track Infrared Sounder (CrIS), while a spectrum of the Moon with CrIS is currently in
the pipeline. First comparisons of CrIS Moon spectrum with HIRS observations at sim-
ilar phase angles show excellent agreement with HIRS/2, while the measurements with
HIRS/3 are roughly 10% lower than the spectrum with CrIS. This confirms that the FOV
was previously underestimated with 1.3° and is even more likely to be $(1.36 \pm 0.05)°$.

Other instruments like Infrared Atmospheric Sounding Interferometer (IASI) or
Geostationary Interferometric Infrared Sounder (GIIRS) could also take spectra of the
Moon and compare it to the HIRS measurements and the TPM to use it for calibration.
In addition to spectrometers, the Spinning Enhanced Visible InfraRed Imager (SEVIRI)
measures at similar wavelengths like HIRS. SEVIRI is an instrument on a geostation-
ary orbit with 11 IR channels measuring between 0.6 and 13.4 μm [WMO OSCAR, 2022].
With SEVIRI it is possible to observe the Moon at phase angles larger than 90°, hence an
extended validation of the TPM would be possible. However, the model will be impor-
tant not only for recalibrating existing IR satellite observation data for climate research
applications, but also for future HIRS-like sensors for which absolute radiometric ac-
curacy and stability are crucial. If upcoming climate satellite missions like Far-infrared
Outgoing Radiation Understanding and Monitoring (FORUM) would use the Moon for
calibration and compare it to the TPM, they would no longer need an internal blackbody
target. Thermal IR instruments on weather satellites and interplanetary missions use the
Moon as an in-flight calibrator to improve the knowledge of beam characteristics or to
verify detector response and linearity [Müller et al., 2021]. Of particular interest is the
potential for intermediate calibration and verification of photometric stability of instru-
ments on weather satellites. Calibration of HIRS with the Moon requires no spacecraft
maneuvers and spans operational lifetime.

A. Appendix

A.1. HIRS instrument characteristics

In the following, instrument properties for all satellites with HIRS/2, HIRS/3 and HIRS/4 are listed. The complete meta data for all satellites can also be found on Zenodo (see Seibert [2022b]), where information like the central wavelength, the calibration coefficients and the FOV for each IR channel of HIRS are listed.

Table A.1.: HIRS/2 spectral characteristics of IR channel on TIROS-N and NOAA-06. Values equivalent for both satellites except for the Noise Equivalent Delta Radiance, whereby the first value stands for TIROS-N and the second value for NOAA-06. Values from Koenig et. al. [1979].

Channel	Half Power Bandwidth [1/cm]	Noise Equivalent Delta Radiance (NEΔN) [m W/m^2 sr cm^{-1}]
1	3	2.56/2.47
2	10	0.46/0.63
3	12	0.53/0.49
4	16	0.30/0.34
5	16	0.19/0.31
6	16	0.24/0.35
7	16	0.14/0.20
8	35	0.058/0.068
9	25	0.030/0.082
10	60	0.15/0.16
11	40	0.14/0.21
12	80	0.19/0.17
13	23	0.0057/0.0032
14	23	0.0031/0.0039
15	23	0.0033/0.0045
16	23	0.0018/0.0027
17	28	0.0021/0.0026
18	35	0.0024/0.0012
19	100	0.0007/0.00062

Table A.2.: HIRS/3 and HIRS/4 spectral characteristics. Values from Robel and Grau-
mann [2014].

Channel	Half Power Bandwidth [1/cm]	Noise Equivalent Delta Radiance (NEΔN) [m W/m^2 sr cm^{-1}]
1	3	3.00
2	10	0.67
3	12	0.50
4	16	0.31
5	16	0.21
6	16	0.24
7	16	0.20
8	35	0.10
9	25	0.15
10	16	0.15
11	40	0.20
12	55	0.20
13	23	0.006
14	23	0.003
15	23	0.004
16	23	0.004
17	28	0.002
18	35	0.002
19	100	0.001

Table A.3.: Properties of HIRS/2 on TIROS-N. Wavenumber values from `https://nwp-saf.eumetsat.int/downloads/rtcoef_rttov13/ir_srf/rtcoef_noaa_5_hirs_srf.html` and FOV values from Koenig et. al. [1979]. For some channels the FOV data was unobtainable in the final HIRS/2 configuration.

Channel	Wavenumber [1/cm]	Wavelength [micron]	FOV [deg]
1	668.58	14.96	-
2	678.86	14.73	-
3	690.80	14.48	1.18
4	703.48	14.22	1.17
5	716.04	13.97	1.18
6	732.09	13.66	1.18
7	747.57	13.38	1.19
8	898.03	11.14	1.20
9	1028.44	9.72	1.21
10	1215.27	8.23	1.21
11	1363.18	7.34	1.20
12	1484.47	6.74	-
13	2190.93	4.56	-
14	2211.89	4.52	-
15	2239.53	4.47	-
16	2274.89	4.40	-
17	2359.98	4.24	-
18	2510.98	3.98	1.23
19	2667.06	3.75	1.24

Table A.4.: Properties of HIRS/2 on NOAA-06. Wavenumber values from `https://nwp-saf.eumetsat.int/downloads/rtcoef_rttov13/ir_srf/rtcoef_noaa_6_hirs-shifted_srf.html` **and** FOV values from Koenig et. al. [1979]. For some channels the FOV data was unobtainable in the final HIRS/2 configuration.

Channel	Wavenumber [1/cm]	Wavelength [micron]	FOV [deg]
1	672.21	14.88	-
2	675.90	14.80	-
3	689.88	14.50	1.16
4	704.92	14.19	1.17
5	718.44	13.92	1.17
6	732.31	13.66	1.17
7	749.84	13.34	1.18
8	896.77	11.15	1.20
9	1020.20	9.80	1.21
10	1222.63	8.18	1.20
11	1366.13	7.32	1.20
12	1481.51	6.75	1.19
13	2190.49	4.57	1.23
14	2210.86	4.52	1.23
15	2237.61	4.47	1.23
16	2269.66	4.41	1.23
17	2360.94	4.24	1.22
18	2515.27	3.98	1.24
19	2650.04	3.77	1.22

Table A.5.: Properties of HIRS/2 on NOAA-07. Wavenumber values from `https://nwp-saf.eumetsat.int/downloads/rtcoef_rttov13/ir_srf/rtcoef_noaa_7_hirs-shifted_srf.html` and FOV values from Burgdorf et al. [2020].

Channel	Wavenumber [1/cm]	Wavelength [micron]	FOV [deg]
1	671.85	14.88	1.4
2	676.13	14.79	1.4
3	692.81	14.43	1.4
4	704.43	14.20	1.4
5	717.33	13.94	1.4
6	733.76	13.63	1.4
7	750.83	13.32	1.4
8	897.88	11.14	1.4
9	1019.03	9.81	1.4
10	1221.48	8.19	1.4
11	1360.54	7.35	1.4
12	1485.07	6.73	1.4
13	2182.31	4.58	1.4
14	2206.92	4.53	1.4
15	2239.95	4.46	1.4
16	2270.85	4.40	1.4
17	2357.17	4.24	1.4
18	2513.99	3.98	1.4
19	2652.77	3.77	1.4

Table A.6.: Properties of HIRS/2 on NOAA-08. Wavenumber values from `https://nwp-saf.eumetsat.int/downloads/rtcoef_rttov13/ir_srf/rtcoef_noaa_8_hirs-shifted_srf.html` and FOV values from Burgdorf et al. [2020].

Channel	Wavenumber [1/cm]	Wavelength [micron]	FOV [deg]
1	674.48	14.83	1.4
2	674.06	14.84	1.4
3	692.02	14.45	1.4
4	703.70	14.21	1.4
5	717.28	13.94	1.4
6	732.15	13.66	1.4
7	747.77	13.37	1.4
8	897.38	11.14	1.4
9	1019.65	9.81	1.4
10	1220.96	8.19	1.4
11	1361.45	7.35	1.4
12	1482.52	6.75	1.4
13	2188.20	4.57	1.4
14	2210.32	4.52	1.4
15	2238.24	4.47	1.4
16	2271.12	4.40	1.4
17	2357.24	4.24	1.4
18	2514.75	3.98	1.4
19	2656.38	3.76	1.4

Table A.7.: Properties of HIRS/2 on NOAA-09. Wavenumber values from `https://nwp-saf.eumetsat.int/downloads/rtcoef_rttov13/ ir_srf/rtcoef_noaa_9_hirs-shifted_srf.html` and FOV values from Burgdorf et al. [2020].

Channel	Wavenumber [1/cm]	Wavelength [micron]	FOV [deg]
1	671.66	14.89	1.4
2	677.13	14.77	1.4
3	692.31	14.44	1.4
4	703.93	14.21	1.4
5	719.87	13.89	1.4
6	732.92	13.64	1.4
7	749.16	13.35	1.4
8	899.76	11.11	1.4
9	1024.86	9.76	1.4
10	1220.15	8.20	1.4
11	1362.54	7.34	1.4
12	1484.49	6.74	1.4
13	2190.68	4.56	1.4
14	2209.68	4.53	1.4
15	2242.88	4.46	1.4
16	2274.55	4.40	1.4
17	2359.85	4.24	1.4
18	2517.16	3.97	1.4
19	2663.48	3.75	1.4

Table A.8.: Properties of HIRS/2 on NOAA-10. Wavenumber values from `https://nwp-saf.eumetsat.int/downloads/rtcoef_rttov13/ir_srf/rtcoef_noaa_10_hirs-shifted_srf.html` and FOV values from Burgdorf et al. [2020].

Channel	Wavenumber [1/cm]	Wavelength [micron]	FOV [deg]
1	672.36	14.87	1.4
2	677.15	14.77	1.4
3	691.50	14.46	1.4
4	705.41	14.18	1.4
5	718.30	13.92	1.4
6	732.95	13.64	1.4
7	749.58	13.34	1.4
8	900.42	11.11	1.4
9	1024.87	9.76	1.4
10	1223.60	8.17	1.4
11	1359.35	7.36	1.4
12	1486.36	6.73	1.4
13	2189.65	4.57	1.4
14	2206.69	4.53	1.4
15	2239.52	4.47	1.4
16	2268.19	4.41	1.4
17	2359.04	4.24	1.4
18	2512.99	3.98	1.4
19	2659.85	3.76	1.4

Table A.9.: Properties of HIRS/2 on NOAA-11. Wavenumber values from `https://nwp-saf.eumetsat.int/downloads/rtcoef_rttov13/ ir_srf/rtcoef_noaa_11_hirs-shifted_srf.html` and FOV values from Burgdorf et al. [2020].

Channel	Wavenumber [1/cm]	Wavelength [micron]	FOV [deg]
1	673.30	14.85	1.4
2	678.85	14.73	1.4
3	690.21	14.49	1.4
4	705.09	14.18	1.4
5	718.94	13.91	1.4
6	732.15	13.66	1.4
7	749.60	13.34	1.4
8	901.84	11.09	1.4
9	1027.45	9.73	1.4
10	795.85	12.57	1.4
11	1358.33	7.36	1.4
12	1484.17	6.74	1.4
13	2190.04	4.57	1.4
14	2209.72	4.53	1.4
15	2239.32	4.47	1.4
16	2267.95	4.41	1.4
17	2416.54	4.14	1.4
18	2511.99	3.98	1.4
19	2664.33	3.75	1.4

Table A.10.: Properties of HIRS/2 on NOAA-12. Wavenumber values from `https://nwp-saf.eumetsat.int/downloads/rtcoef_rttov13/ir_srf/rtcoef_noaa_12_hirs-shifted_srf.html` and FOV values from Burgdorf et al. [2020].

Channel	Wavenumber [1/cm]	Wavelength [micron]	FOV [deg]
1	669.44	14.94	1.4
2	679.50	14.72	1.4
3	689.68	14.50	1.4
4	704.68	14.19	1.4
5	718.57	13.92	1.4
6	732.30	13.66	1.4
7	749.74	13.34	1.4
8	899.80	11.11	1.4
9	1026.31	9.74	1.4
10	1221.27	8.19	1.4
11	1361.56	7.34	1.4
12	1484.72	6.74	1.4
13	2188.45	4.57	1.4
14	2210.60	4.52	1.4
15	2238.50	4.47	1.4
16	2267.69	4.41	1.4
17	2361.62	4.23	1.4
18	2514.67	3.98	1.4
19	2653.60	3.77	1.4

Table A.11.: Properties of HIRS/2 on NOAA-14. Wavenumber values from `https://nwp-saf.eumetsat.int/downloads/rtcoef_rttov13/ir_srf/rtcoef_noaa_14_hirs-shifted_srf.html` and FOV values from Burgdorf et al. [2020].

Channel	Wavenumber [1/cm]	Wavelength [micron]	FOV [deg]
1	668.66	14.96	1.4
2	680.21	14.70	1.4
3	690.27	14.49	1.4
4	705.64	14.17	1.4
5	717.81	13.93	1.4
6	732.28	13.66	1.4
7	750.90	13.32	1.4
8	899.34	11.12	1.4
9	1028.30	9.72	1.4
10	799.46	12.51	1.4
11	1351.81	7.40	1.4
12	1485.13	6.73	1.4
13	2191.31	4.56	1.4
14	2207.35	4.53	1.4
15	2236.31	4.47	1.4
16	2268.16	4.41	1.4
17	2420.38	4.13	1.4
18	2512.27	3.98	1.4
19	2648.34	3.78	1.4

Table A.12.: Properties of HIRS/3 on NOAA-15. Wavenumber values from `https://nwp-saf.eumetsat.int/downloads/rtcoef_rttov13/ir_srf/rtcoef_noaa_15_hirs-shifted_srf.html` and FOV values from Burgdorf et al. [2020].

Channel	Wavenumber [1/cm]	Wavelength [micron]	FOV [deg]
1	667.72	14.98	1.3
2	678.30	14.74	1.3
3	689.26	14.51	1.3
4	702.94	14.23	1.3
5	716.20	13.96	1.3
6	731.74	13.67	1.3
7	748.67	13.36	1.3
8	896.74	11.15	1.3
9	1030.37	9.71	1.3
10	803.59	12.44	1.3
11	1369.29	7.30	1.3
12	1530.42	6.53	1.3
13	2188.19	4.57	1.3
14	2209.94	4.53	1.3
15	2235.28	4.47	1.3
16	2241.98	4.46	1.3
17	2418.98	4.13	1.3
18	2518.80	3.97	1.3
19	2657.27	3.76	1.3

Table A.13.: Properties of HIRS/3 on NOAA-16. Wavenumber values from `https://nwp-saf.eumetsat.int/downloads/rtcoef_rttov13/ir_srf/rtcoef_noaa_16_hirs-shifted_srf.html` and FOV values from Burgdorf et al. [2020].

Channel	Wavenumber [1/cm]	Wavelength [micron]	FOV [deg]
1	669.24	14.94	1.3
2	679.53	14.72	1.3
3	690.23	14.49	1.3
4	702.08	14.24	1.3
5	717.20	13.94	1.3
6	731.34	13.67	1.3
7	750.25	13.33	1.3
8	897.40	11.14	1.3
9	1030.14	9.71	1.3
10	805.76	12.41	1.3
11	1369.42	7.30	1.3
12	1527.68	6.55	1.3
13	2186.95	4.57	1.3
14	2206.48	4.53	1.3
15	2233.30	4.48	1.3
16	2242.85	4.46	1.3
17	2417.95	4.14	1.3
18	2517.83	3.97	1.3
19	2666.27	3.75	1.3

Table A.14.: Properties of HIRS/3 on NOAA-17. Wavenumber values from `https://nwp-saf.eumetsat.int/downloads/rtcoef_rttov13/ir_srf/rtcoef_noaa_17_hirs-shifted_srf.html` and FOV values from Burgdorf et al. [2020].

Channel	Wavenumber [1/cm]	Wavelength [micron]	FOV [deg]
1	668.19	14.97	1.3
2	681.70	14.67	1.3
3	690.92	14.47	1.3
4	703.27	14.22	1.3
5	716.45	13.96	1.3
6	731.83	13.66	1.3
7	748.48	13.36	1.3
8	899.03	11.12	1.3
9	1028.60	9.72	1.3
10	804.52	12.43	1.3
11	1366.18	7.32	1.3
12	1527.47	6.55	1.3
13	2185.58	4.58	1.3
14	2210.98	4.52	1.3
15	2232.99	4.48	1.3
16	2240.38	4.46	1.3
17	2416.91	4.14	1.3
18	2519.10	3.97	1.3
19	2657.55	3.76	1.3

Table A.15.: Properties of HIRS/4 on NOAA-18. Wavenumber values from `https://nwp-saf.eumetsat.int/downloads/rtcoef_rttov13/ir_srf/rtcoef_noaa_18_hirs-shifted_srf.html` and FOV values from Burgdorf et al. [2020].

Channel	Wavenumber [1/cm]	Wavelength [micron]	FOV [deg]
1	667.58	14.98	0.7
2	680.43	14.70	0.7
3	689.06	14.51	0.7
4	703.10	14.22	0.7
5	713.97	14.01	0.7
6	731.54	13.67	0.7
7	749.65	13.34	0.7
8	899.49	11.12	0.7
9	1028.81	9.72	0.7
10	799.91	12.50	0.7
11	1367.22	7.31	0.7
12	1535.47	6.51	0.7
13	2189.22	4.57	0.7
14	2208.45	4.53	0.7
15	2238.36	4.47	0.7
16	2246.65	4.45	0.7
17	2419.16	4.13	0.7
18	2515.42	3.98	0.7
19	2666.14	3.75	0.7

Table A.16.: Properties of HIRS/4 on NOAA-19. Wavenumber values from `https://nwp-saf.eumetsat.int/downloads/rtcoef_rttov13/ir_srf/rtcoef_noaa_19_hirs-shifted_srf.html` and FOV values from Burgdorf et al. [2020].

Channel	Wavenumber [1/cm]	Wavelength [micron]	FOV [deg]
1	668.78	14.95	0.7
2	680.95	14.69	0.7
3	688.43	14.53	0.7
4	702.64	14.23	0.7
5	715.68	13.97	0.7
6	733.39	13.64	0.7
7	749.22	13.35	0.7
8	898.99	11.12	0.7
9	1027.87	9.73	0.7
10	802.80	12.46	0.7
11	1360.20	7.35	0.7
12	1531.74	6.53	0.7
13	2185.02	4.58	0.7
14	2213.95	4.52	0.7
15	2232.65	4.48	0.7
16	2246.86	4.45	0.7
17	2420.81	4.13	0.7
18	2518.41	3.97	0.7
19	2661.92	3.76	0.7

Table A.17.: Properties of HIRS/4 on Metop-A. Wavenumber values from `https://nwp-saf.eumetsat.int/downloads/rtcoef_rttov13/ir_srf/rtcoef_metop_1_hirs-shifted_srf.html` and FOV values from ITT Exelis [2012].

Channel	Wavenumber [1/cm]	Wavelength [micron]	FOV [deg]
1	668.66	14.96	0.671
2	679.37	14.72	0.675
3	689.53	14.50	0.675
4	701.84	14.25	0.677
5	716.57	13.96	0.677
6	731.71	13.67	0.677
7	748.67	13.36	0.676
8	898.07	11.13	0.681
9	1028.31	9.72	0.683
10	800.86	12.49	0.675
11	1362.12	7.34	0.685
12	1532.33	6.53	0.685
13	2189.72	4.57	0.655
14	2212.33	4.52	0.659
15	2237.61	4.47	0.658
16	2245.57	4.45	0.659
17	2418.86	4.13	0.666
18	2516.06	3.97	0.669
19	2663.68	3.75	0.673

Table A.18.: Properties of HIRS/4 on Metop-B. Wavenumber values from `https://nwp-saf.eumetsat.int/downloads/rtcoef_rttov13/ir_srf/rtcoef_metop_2_hirs-shifted_srf.html` and FOV values from ITT Exelis [2012].

Channel	Wavenumber [1/cm]	Wavelength [micron]	FOV [deg]
1	668.28	14.96	0.671
2	680.82	14.69	0.675
3	690.90	14.47	0.675
4	701.87	14.25	0.677
5	714.51	14.00	0.677
6	731.45	13.67	0.677
7	746.82	13.39	0.676
8	898.73	11.13	0.681
9	1029.36	9.71	0.683
10	803.98	12.44	0.675
11	1359.70	7.35	0.685
12	1533.60	6.52	0.685
13	2185.71	4.58	0.655
14	2206.64	4.53	0.659
15	2234.18	4.48	0.658
16	2242.95	4.46	0.659
17	2421.05	4.13	0.666
18	2515.97	3.97	0.669
19	2664.83	3.75	0.673

A.2. Comparison of moon intrusions with the TPM
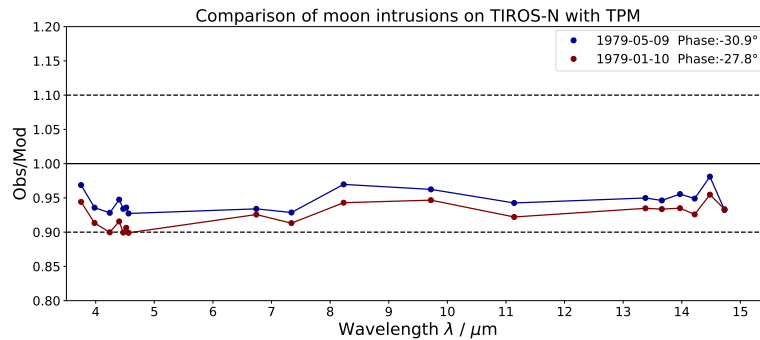
Figure A.1.: Moon observations with HIRS divided by the TPM calculations in depen-
dence of the wavelength on TIROS-N. Each color is a different moon obser-
vation. The dashed horizontal lines represent the +/-10% difference of the
observations and the model.
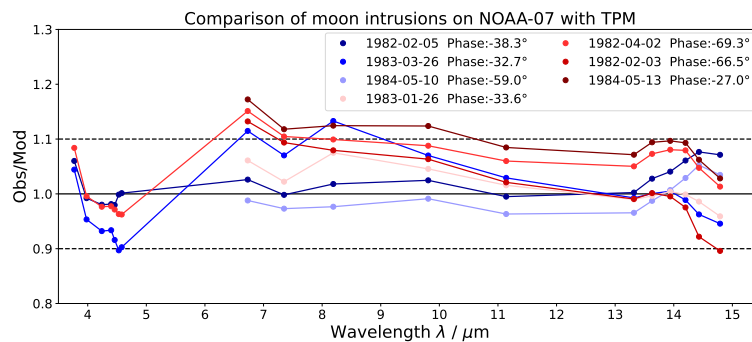
Figure A.2.: Moon observations with HIRS divided by the TPM calculations in depen-
dence of the wavelength on NOAA-07. Each color is a different moon obser-
vation. The dashed horizontal lines represent the +/-10% difference of the
observations and the model.
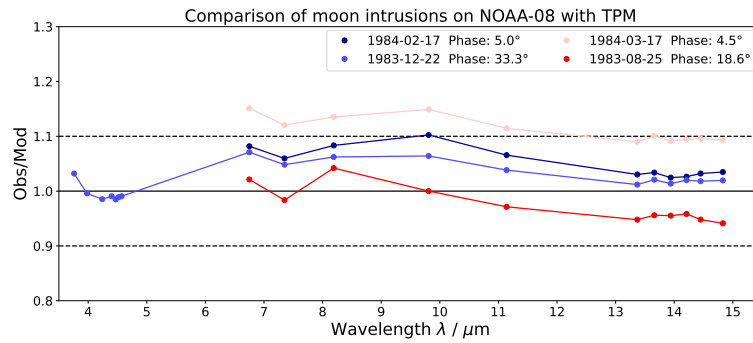
Figure A.3.: Moon observations with HIRS divided by the TPM calculations in dependence of the wavelength on NOAA-08. Each color is a different moon observation. The dashed horizontal lines represent the +/-10% difference of the observations and the model.
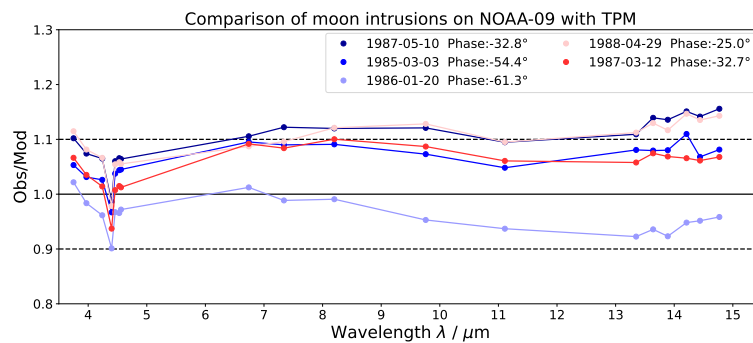
Figure A.4.: Moon observations with HIRS divided by the TPM calculations in dependence of the wavelength on NOAA-09. Each color is a different moon observation. The dashed horizontal lines represent the +/-10% difference of the observations and the model.
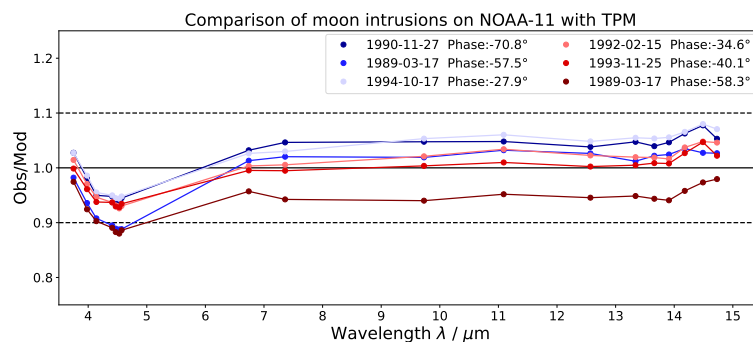
Figure A.5.: Moon observations with HIRS divided by the TPM calculations in dependence of the wavelength on NOAA-11. Each color is a different moon observation. The dashed horizontal lines represent the +/-10% difference of the observations and the model.
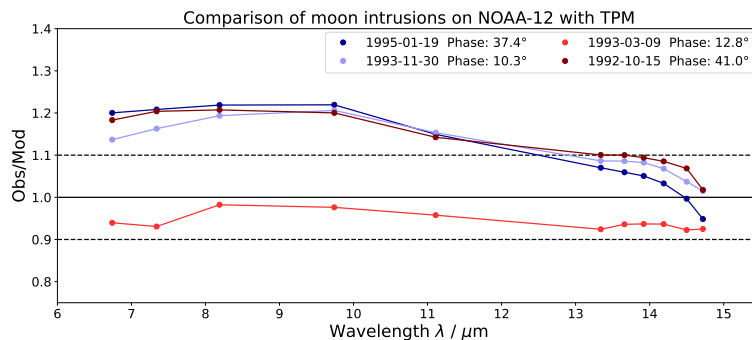
Figure A.6.: Moon observations with HIRS divided by the TPM calculations in dependence of the wavelength on NOAA-12. Each color is a different moon observation. The dashed horizontal lines represent the +/-10% difference of the observations and the model.
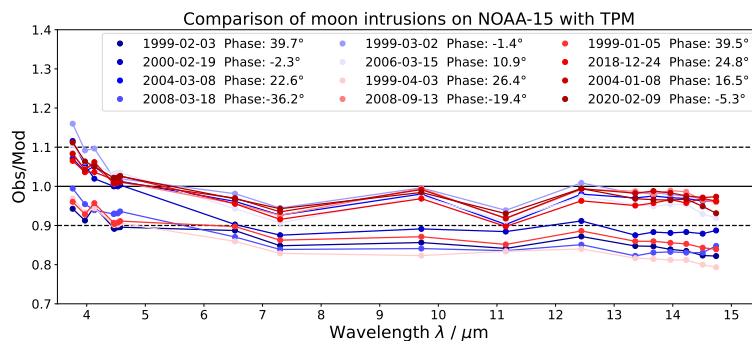
Figure A.7.: Moon observations with HIRS divided by the TPM calculations in dependence of the wavelength on NOAA-15. Each color is a different moon observation. The dashed horizontal line represent the -10% difference of the observations and the model.
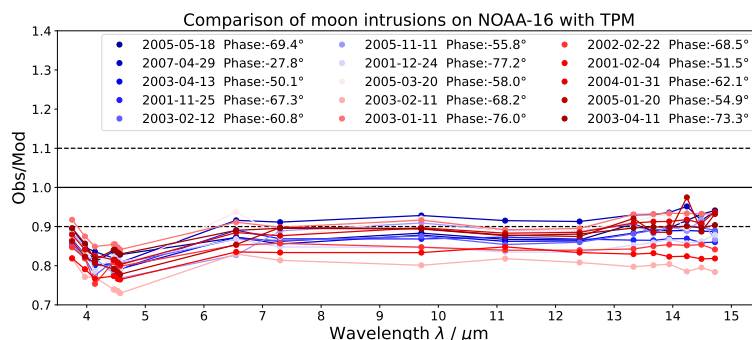
Figure A.8.: Moon observations with HIRS divided by the TPM calculations in dependence of the wavelength on NOAA-16. Each color is a different moon observation. The dashed horizontal line represent the -10% difference of the observations and the model.
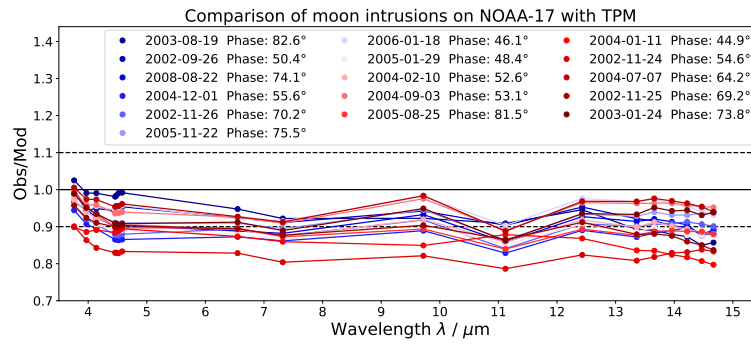
Figure A.9.: Moon observations with HIRS divided by the TPM calculations in dependence of the wavelength on NOAA-17. Each color is a different moon observation. The dashed horizontal lines represent the +/-10% difference of the observations and the model.
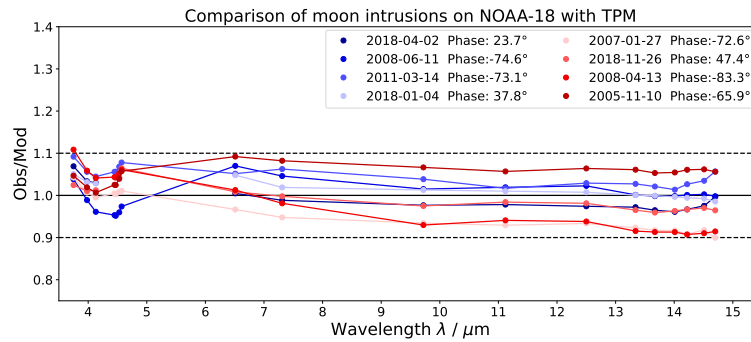
Figure A.10.: Moon observations with HIRS divided by the TPM calculations in dependence of the wavelength on NOAA-18. Each color is a different moon observation. The dashed horizontal lines represent the +/-10% difference of the observations and the model.
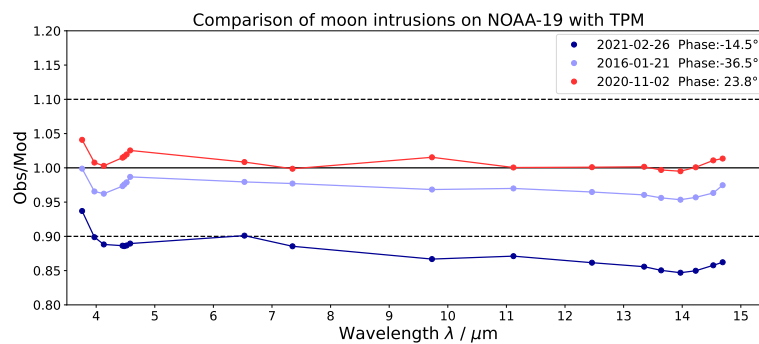
Figure A.11.: Moon observations with HIRS divided by the TPM calculations in dependence of the wavelength on NOAA-19. Each color is a different moon observation. The dashed horizontal lines represent the +/-10% difference of the observations and the model.
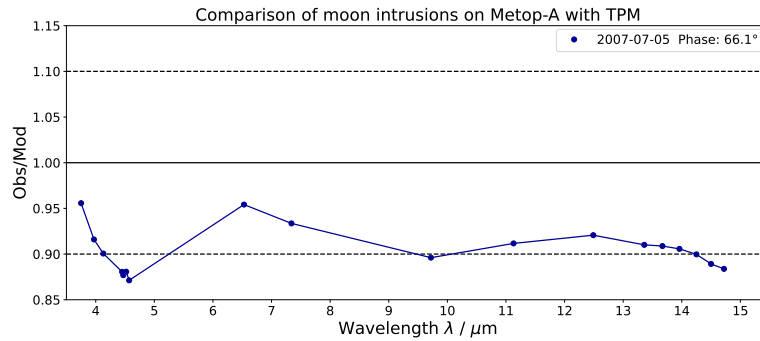
Figure A.12.: Moon observations with HIRS divided by the TPM calculations in depen-
dence of the wavelength on Metop-A. Each color is a different moon obser-
vation. The dashed horizontal lines represent the +/-10% difference of the
observations and the model.
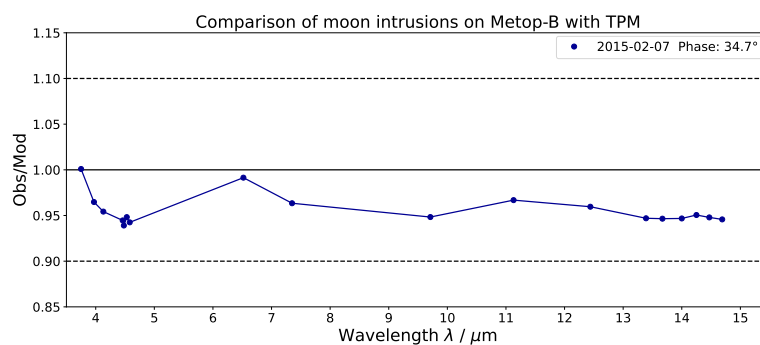
Figure A.13.: Moon observations with HIRS divided by the TPM calculations in depen-
dence of the wavelength on Metop-B. Each color is a different moon obser-
vation. The dashed horizontal lines represent the +/-10% difference of the
observations and the model.

List of Figures

List of Tables

Bibliography

Astronomy Notes. Phases and Eclipses. `https://www.astronomynotes.com/nakedeye/s13.htm`, accessed on 09 March 2022.

S. A. Buehler, M. Prange, J. Mrziglod, V. O. John, M. Burgdorf, and O. Lemke. Opportunistic Constant Target Matching—A New Method for Satellite Intercalibration. *Earth and Space Science*, 7(5):e2019EA000856, 2020. doi: https://doi.org/10.1029/2019EA000856. URL `https://agupubs.onlinelibrary.wiley.com/doi/abs/10.1029/2019EA000856`. e2019EA000856 10.1029/2019EA000856.

M. Burgdorf, S. A. Buehler, T. Lang, S. Michel, and I. Hans. The Moon as a photometric calibration standard for microwave sensors. *Atmospheric Measurement Techniques*, 9(8): 3467–3475, 2016. doi: 10.5194/amt-9-3467-2016. URL `https://amt.copernicus.org/articles/9/3467/2016/`.

M. J. Burgdorf, T. G. Müller, S. A. Buehler, M. Prange, and M. Brath. Characterization of the High-Resolution Infrared Radiation Sounder Using Lunar Observations. *Remote Sensing*, 12(9), 2020. ISSN 2072-4292. doi: 10.3390/rs12091488. URL `https://www.mdpi.com/2072-4292/12/9/1488`.

C. Cao, H. Xu, J. Sullivan, L. McMillin, P. Ciren, and Y. Hou. Intersatellite Radiance Biases for the High-Resolution Infrared Radiation Sounders (HIRS) on board NOAA-15, -16, and -17 from Simultaneous Nadir Observations. *Journal of Atmospheric and Oceanic Technology*, 22(4):381 – 395, 2005. doi: 10.1175/JTECH1713.1. URL `https://journals.ametsoc.org/view/journals/atot/22/4/jtech1713_1.xml`.

Y. Chen, D. Tremblay, L. Wang, and F. Iturbide-Sanchez. Improved Lunar Intrusion Detection Algorithm for the CrIS Sensor Data Record. *IEEE Transactions on Geoscience and Remote Sensing*, 58(2):1134–1145, 2020. doi: 10.1109/TGRS.2019.2944003.

K. Gierens, K. Eleftheratos, and R. Sausen. Intercalibration between HIRS/2 and HIRS/3 channel 12 based on physical considerations. *Atmospheric Measurement Techniques*, 11 (2):939–948, 2018. doi: 10.5194/amt-11-939-2018. URL `https://amt.copernicus.org/articles/11/939/2018/`.

I. M. Held and B. J. Soden. Water Vapor Feedback and Global Warming. *Annual Review of Energy and the Environment*, 25(1):441–475, 2000. doi: 10.1146/annurev.energy.25.1.441. URL `https://doi.org/10.1146/annurev.energy.25.1.441`.

G. Holl, J. P. D. Mittaz, and C. J. Merchant. Error Correlations in High-Resolution Infrared Radiation Sounder (HIRS) Radiances. *Remote Sensing*, 11(11), 2019. ISSN 2072-4292. doi: 10.3390/rs11111337. URL `https://www.mdpi.com/2072-4292/11/11/1337`.

G.-P. Hu, Y.-C. Zheng, A.-A. Xu, and Z.-S. Tang. Microwave Brightness Temperature of the Moon: The Possibility of Setting a Calibration Source of the Lunar Surface. *IEEE Geoscience and Remote Sensing Letters*, 13:1–5, 01 2015. doi: 10.1109/LGRS.2015.2504543.

Geospatial Systems ITT Exelis. *Instruction Manual and Alignment/Calibration Handbook & Optical Data for the High Resolution Infrared Radiation Sounder HIRS/4 S/N H307*. National Oceanic and Atmospheric Administration, 2012.

K. B. Kidwell. *NOAA Polar Orbiter Users Guide (TIROS-N, NOAA-6, NOAA-7, NOAA-8, NOAA-9, NOAA-10, NOAA-11, NOAA-12, NOAA-13, and NOAA-14)*. National Oceanic and Atmospheric Administration, 1995.

H. H. Kieffer and R. L. Wildey. Establishing the Moon as a Spectral Radiance Standard. *Journal of Atmospheric and Oceanic Technology*, 13(2):360 – 375, 1996. doi: 10.1175/1520-0426(1996)013<0360:ETMAAS>2.0.CO;2. URL `https://journals.ametsoc.org/view/journals/atot/13/2/1520-0426_1996_013_0360_etmaas_2_0_co_2.xml`.

E. W. Koenig. *Performance of the HIRS/2 Instrument on TIROS-N*, page 67–94. Academic Press, 1980.

E. W. Koenig et. al. *High Resolution Infrared Radiation Sounder (HIRS) for the Nimbus F Spacecraft*. NASA Goddard Space Flight Center (ITT Aerospace/Optical Div. Fort Wayne, IN, United States), 1975.

E. W. Koenig et. al. *High Resolution Infrared Radiation Sounder/MOD 2 (HIRS/2)*. NASA Goddard Space Flight Center (ITT Aerospace/Optical Div. Fort Wayne, IN, United States), 1979.

T. Labrot, L. Lavanant, K. Whyte, N. Atkinson, and P. Brunel. *AAPP Documentation Scientific Description*. Satellite Application Facility for Numerical Wheather Prediction, 2011. URL `https://nwp-saf.eumetsat.int/site/software/aapp/`.

J. S. V. Lagerros. Thermal physics of asteroids. I. Effects of shape, heat conduction and beaming. *Astronomy and Astrophysics*, 310:1011–1020, June 1996.

J. S. V. Lagerros. Thermal physics of asteroids. III. Irregular shapes and albedo variegations. *Astronomy and Astrophysics*, 325:1226–1236, September 1997.

J. S. V. Lagerros. Thermal physics of asteroids. IV. Thermal infrared beaming. *Astronomy and Astrophysics*, 332:1123–1132, April 1998.

O. Lemke, L. Kluft, J. Mrziglod, S. Pfreundschuh, G. Holl, R. Larsson, T. Yamada, T. Mieslinger, and J. Doerr. atmtools/typhon: Typhon release 0.9.0, December 2021. URL `https://doi.org/10.5281/zenodo.5786028`.

N. Liu and Y. Jin. Average Infrared Brightness Temperature of Lunar Rough Surface in Field of View of High-Resolution Infrared Radiation Sounder and Application to Calibration. *IEEE Transactions on Geoscience and Remote Sensing*, 60:1–12, 2022. doi: 10.1109/TGRS.2021.3094106.

T. G. Müller. Thermophysical analysis of infrared observations of asteroids. *Meteoritics & Planetary Science*, 37(12):1919–1928, December 2002. doi: 10.1111/j.1945-5100.2002. tb01173.x.

T. G. Müller and J. S. V. Lagerros. Asteroids as far-infrared photometric standards for ISOPHOT. *Astronomy and Astrophysics*, 338:340–352, October 1998.

T. G. Müller and J. S. V. Lagerros. Asteroids as calibration standards in the thermal infrared for space observatories. *Astronomy and Astrophysics*, 381:324–339, January 2002. doi: 10.1051/0004-6361:20011491.

T. G. Müller, M. Burgdorf, V. Alí-Lagoa, S. A. Buehler, and M. Prange. The moon at thermal infrared wavelengths: a benchmark for asteroid thermal models. *A&A*, 650: A38, 2021. doi: 10.1051/0004-6361/202039946. URL `https://doi.org/10.1051/0004-6361/202039946`.

NASA. JPL Horizons System. `https://ssd.jpl.nasa.gov/horizons/manual.html`, accessed on 25 June 2022.

Remote Sensing Systems. Crossing Times. `https://www.remss.com/support/crossing-times/`, accessed on 22 February 2022.

J. Robel and A. Graumann. *NOAA KLM User's Guide with NOAA-N, N Prime, and MetOp Supplements*. National Oceanic and Atmospheric Administration, 2014.

R. Roebeling, J. Schulz, T. Hewison, and B. Theodore. Inter-calibration of METEOSAT IR and WV channels using HIRS. *AIP Conference Proceedings*, 1531(1):288–291, 2013. doi: 10.1063/1.4804763. URL `https://aip.scitation.org/doi/abs/10.1063/1.4804763`.

C. Seibert. Hirs moon intrusions and model calculations, July 2022a. URL `https://doi.org/10.5281/zenodo.6865664`.

C. Seibert. A collection of instrument characteristics for all satellites with HIRS/2, HIRS/3 and HIRS/4, July 2022b. URL `https://doi.org/10.5281/zenodo.6822188`.

L. Shi and J. J. Bates. Three decades of intersatellite-calibrated High-Resolution Infrared Radiation Sounder upper tropospheric water vapor. *Journal of Geophysical Research: Atmospheres*, 116(D4), 2011. doi: https://doi.org/10.1029/2010JD014847. URL `https://agupubs.onlinelibrary.wiley.com/doi/abs/10.1029/2010JD014847`.

L. Shi, J. J. Bates, and C. Cao. Scene Radiance–Dependent Intersatellite Biases of HIRS Longwave Channels. *Journal of Atmospheric and Oceanic Technology*, 25(12):2219 – 2229, 2008. doi: 10.1175/2008JTECHA1058.1. URL `https://journals.ametsoc.org/view/journals/atot/25/12/2008jtecha1058_1.xml`.

D. Dickinson Universe Today. Earth at aphelion 2016. `https://www.universetoday.com/tag/peribothron/`, accessed on 30 June 2022.

WMO OSCAR. Space-based Capabilities - Instruments. `https://space.oscar.wmo.int/instruments`, accessed on 05 April 2022.

Acknowledgements

Eidesstattliche Versicherung

Hiermit versichere ich an Eides statt, dass ich die vorliegende Arbeit im Studiengang M.Sc. Meteorologie selbstständig verfasst unf keine anderen als die angegebenen Hilfsmittel genutzt habe. Alle Stellen, die wörtlich oder sinngemäß aus Veröffentlichungen entnommen wurden, sind als solche kenntlich gemacht. Ich versichere weiterhin, dass ich die Arbeit vorher nicht in einem anderen Prüfungsverfahren eingereicht habe und die eingereichte schriftliche Fassung der auf dem elektronischen Speichermedium entspricht.

Ich bin mit einer Einstellung in den Bestand der Bibliothek des Fachbereiches einverstanden.

Hamburg, den 20.07.2022 Unterschrift: _____